FACULTY OF SCIENCE
UNIVERSITY OF COPENHAGEN

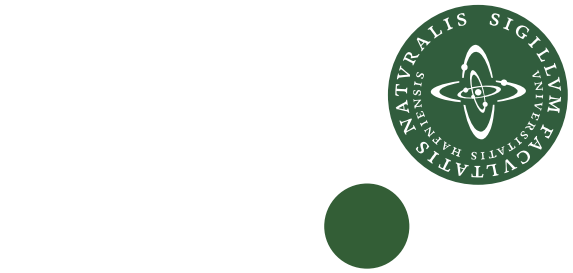

MORPHOLOGICAL STUDY OF HEAVY ION COLLISIONS USING CMB METHODS

MASTER THESIS

by **Anne Mette Frejsel**

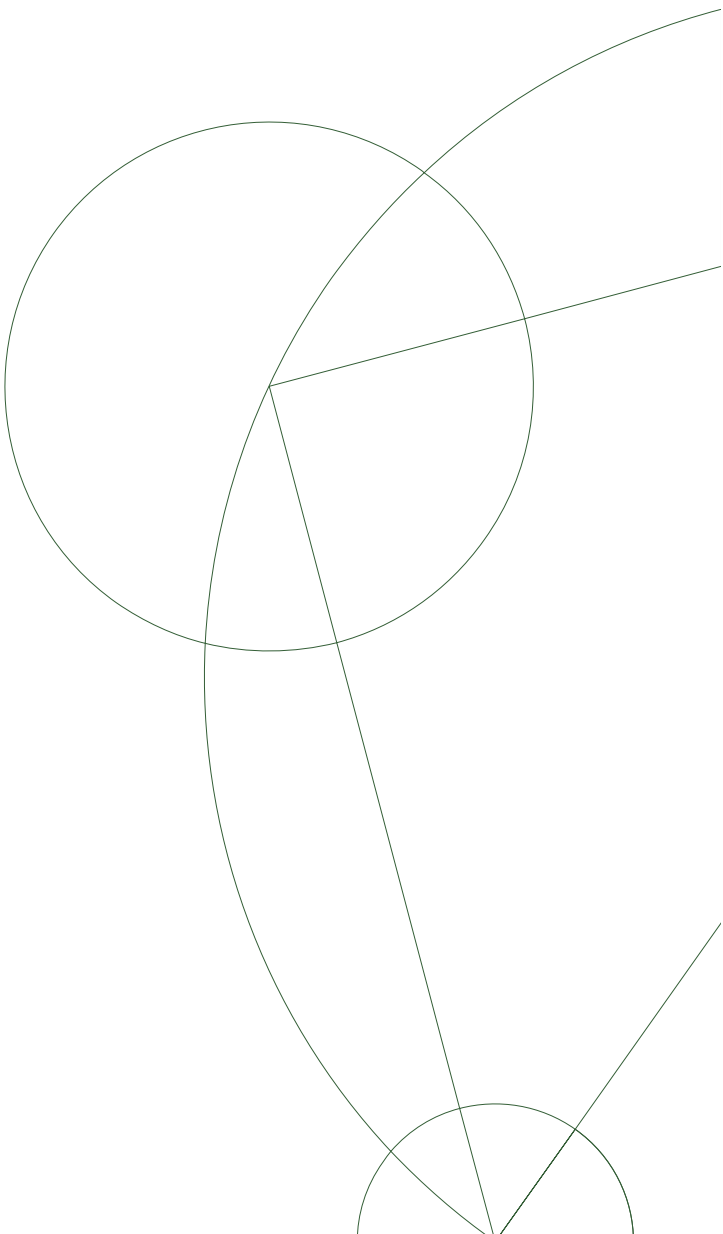

Supervisor:
Pavel Naselsky
Niels Bohr Institute and Discovery Center
Copenhagen University

Submitted: May 18, 2012

Abstract

This thesis implements methods developed for Cosmic Microwave Background (CMB) analysis into the framework of heavy ion physics. This is done in order to investigate simulations of high-multiplicity heavy ion collisions (events) on an event-by-event basis. A qualitative method for determining the elliptic flow amplitude and the event plane angle on an event-by-event basis is developed. The CMB methods are based on the decomposition of a signal into spherical harmonics. Using the coefficients of the decomposition, called a_{lm}, an analytical formula for extracting information on both odd and even collective flow moments in a heavy ion event is derived. It is shown that elliptic flow is tightly connected to the a_{22} coefficient. The data analysis is done on both simple toy model simulations and on HIJING (Heavy-Ion Jet INteraction Generator) simulations. A tight linear relationship is seen for both toy model and HIJING simulations (as predicted from the analytical formula). The methods developed here should be applicable for higher order flow as well.

Resume

Dette speciale tager udgangspunkt i metoder der er udviklet til analyse af den kosmiske mikrobølge-baggrundsstråling (CMB) og implementerer dem i tung-ions fysik. Formålet er at studere simuleringer af høj-multiplicitets tung-ions kollisioner pået event-per-event grundlag. En kvalitativ metode til event-per-event bestemmelse af amplituden af elliptisk flow og event plane angle udledes. CMB metoderne er baseret p transformationen af et signal til spherical harmonics. Ved at benytte koefficienterne for denne transformation, kaldet a_{lm}, udledes en analytisk formel for lige og ulige momenter af kollektivt flow i en tung-ions kollision. Det vises, at elliptisk flow er tæt forbundet til a_{22} koefficienten. Dataanalysen er udført både p simuleringer lavet med en forsimplet model og p HIJING (Heavy-Ion Jet INteraction Generator) simuleringer. En tæt lineær sammenhng (som forudsagt af den analytiske formel) ses for bde den simple model og HIJING simuleringer. De udviklede metoder bør ogsåkunne anvendes for højere ordens flow.

Contents

Preface

The idea for the investigation of the topic of this thesis was born at the Discovery Center at the Niels Bohr Institute in 2011. I have had the pleasure of being part of the work since the very beginning and working together with many different people in the process. The project has resulted in an article, which at this time has been submitted to Physical Review C. Some of the work in this thesis is thus also part of:
P. Naselsky et al., *Morphology of High-Multiplicity Events in Heavy Ion Collisions*, 2012 [1].

I hope you will enjoy reading this thesis, just as I have enjoyed working on this interesting subject.

Acknowledgements

I would like to thank the Planck group of the Discovery Center at the Niels Bohr Institute, in particular my supervisor Pavel Naselsky for letting me be part of this project and sharing his knowledge on many a subject. I would like to thank Per Rex Christensen from the group for helping me with valuable advice and insight, as well as his contributions to the paper on this project. I would also like to thank the Heavy Ion group of the Discovery Center, without whom this project would never have been born. In particular I would like to thank Jens Jørgen Gaardhøje, who developed the toy model and simulated the data used in chapter 7 of this thesis, and Alexander C. Hansen who has taken the time to explain many things to me about heavy ion physics, as well as simulating all the data used in chapter 8 of this thesis.

I would also like to thank my other fellow co-authors of the paper: Poul Henrik Damgaard, Urs Wiedemann, Oleg Verkhodanov, Jaiseung Kim, Christian Holm Christensen and Martin Hansen.

I am very grateful to the people who have commented on and proof-read my thesis - it has been a tremendous help.

A special thanks also to my office mate, Martin, who has always been available for valuable discussions and help, and has put up with interruptions and co-procrastination on many occasions. I would also like to thank my fellow Discovery youngsters for many a good coffee break in the M-building, often with interesting discussions (and cake).

Chapter 1

Introduction

The motivation for the topic of this thesis is the idea that knowledge and advances in one field of physics might benefit another - with methods, physics or just the sharing of ideas. The two fields in question here are cosmology - in particular the field of Cosmic Microwave Background (CMB) research, to which the author belongs - and heavy ion physics.

The CMB field has acquired decades of knowledge on performing a statistical analysis of a very smooth spherical signal with small morphological modulations. The heavy ion field on the other hand is growing into the need for detailed analysis of fluctuations on an event-by-event basis instead of doing statistical analysis of a large ensemble of events.

The idea of exploiting the knowledge and tools from CMB physics in the analysis of heavy ion data is thus compelling, and the potential results intriguing. Such an endeavour was undertaken at the Discovery Center at the Niels Bohr Institute at the University of Copenhagen by the CMB and heavy ion groups. The author of this thesis has done much of the data analysis for this collaboration, some of which is part of a paper by the two groups [1]. The paper documents and discusses the findings and potential applications of using standard CMB tools for the analysis of simulated particle distributions of ultra-relativistic heavy ion collisions. There are of course many features of interest in heavy ion collisions, but this thesis - and the paper - limits itself to the study of collective flow. This thesis goes a bit further than the analysis presented in the paper, but an extension of the analysis to real data or detector-acceptance simulations is beyond the scope of this thesis.

The thesis is divided into three parts. Before any direct application of methods can be made a knowledge of how they were developed and for what, as well as background knowledge of the problems one wishes to apply them to is necessary. This is covered in part I. Here chapter 2 gives an extended motivation for the collaboration, pointing out the kinship of CMB physics and heavy ion physics and how the work on the subject should be undertaken. Chapter 3 covers the background of CMB physics, from the theory of the creation of the CMB and the experiments used for its observation, to the applications of the methods in CMB science itself. In chapter 4 the theoretical background of the subject of investigation - collective flow in heavy ion collisions - as well as a brief introduction to the heavy ion field is given.

Once the theoretical framework is set, the actual mathematical methods and computational

tools can be developed and introduced. This is done in part II, which presents the different methods to be implemented in the data analysis. In chapter 5 the basis for the analysis is presented. The method of spherical harmonic decomposition of a signal is introduced, and equations for a qualitative extraction of flow amplitude from data are derived. The aim is a direct relationship between observable parameters and the collective flow. Chapter 6 presents tools used for the data processing.

Part III covers the data analysis on the basis of the methods presented in part II. Firstly, simulations using a toy model are analysed to test if the mathematical tools developed in part II are indeed usable for the data analysis. Then simulations by a more complex generator, HIJING, are taken under consideration.

The hopeful conclusion to this thesis is that the use of methods from the CMB field enables a qualitative characterisation of collective flow in heavy ion collisions on an event-by-event basis.

Part I

Background & Theory

Chapter 2

A cross-field investigation

The particular constellation of cosmology and heavy ion physics is motivated by the fact that the properties of a heavy ion collision share a remarkable kinship with the physics of the earliest Universe. An important feature of a heavy ion collision is the creation of a very dense initial state - the Quark Gluon Plasma (QGP). This state corresponds to the same densities as in the Universe less than 10^{-10} seconds after the Big Bang (see figure 2.1), where the quark gluon soup transitioned to a confined hadron[1] gas [2]. One could make the analogy that heavy ion collision are in fact 'Little Bangs', recreating primordial conditions.

One may go even further than just the QGP in finding similarities between the early Universe and the 'Little Bangs'. The early Universe has left its imprint on photons emitted some $\sim 380,000$ years after the Big Bang, and is observable today through the CMB. The 'Little Bangs' are observable in heavy ion collisions at accelerators today, such as the Large Hadron Collider (LHC). Both are governed by fluid dynamical propagation of fluctuations, albeit at very different scales. Both are signals with a highly symmetrical morphology with fluctuations. The study of fluid dynamical evolution of matter through the CMB has yielded constraints on the contents of the Universe (i.e. visible matter, dark matter and dark energy) and other properties of the evolution of the Universe [3]. The study of the fluid dynamics in heavy ion collisions has revealed that it behaves almost like a perfect fluid with a shear-viscosity to entropy-density ratio that is almost minimal [4, 5].

There are of course also significant differences between studying heavy ion collisions and studying the CMB. The scales involved are extremely different (order 10^{-18}m versus the entire Universe), as are the governing fundamental forces (the strong force versus gravitation and electromagnetism). However, these differences are not so important when discussing the morphology of the signal. More important is the difference between the study of one single event - the Universe - versus the study of an, in principle, infinite amount of events. The tools and methods used for the study of the CMB are developed and optimised for the study of statistical properties and features of a signal, which is not available in any other configurations in nature.

One can think of (at least) two ways in which two fields could contribute to each other. One concerns the physics involved. Perhaps the cosmological knowledge of fluid dynamical perturbations in an expanding system or the physics of the non-linear evolution of structure in

[1] Hadrons are particles composed of two or three quarks.

the Universe could be of use in heavy ion physics? At the moment, the heavy ion community is only in the very beginning of exploring fluid dynamical perturbations in the analysis, so this is indeed possible. The other way is the methods used for the analysis of data. In high energy physics it is possible to generate millions of events each second, providing a sound statistical ensemble for the exploration of the data. Contrary, CMB physics has been optimised for studying one single event and gaining insight into its properties. Heavy ion physics has not had much focus on the study of fluctuations and properties of the collisions on an event-by-event basis, because of the the readily available abundance of data. The methods for doing such an analysis consequently have not been developed. The methods for the CMB analysis, however, have. This is the motivation for trying to implement the use of CMB methods in the study of the morphology of heavy ion collisions [1].

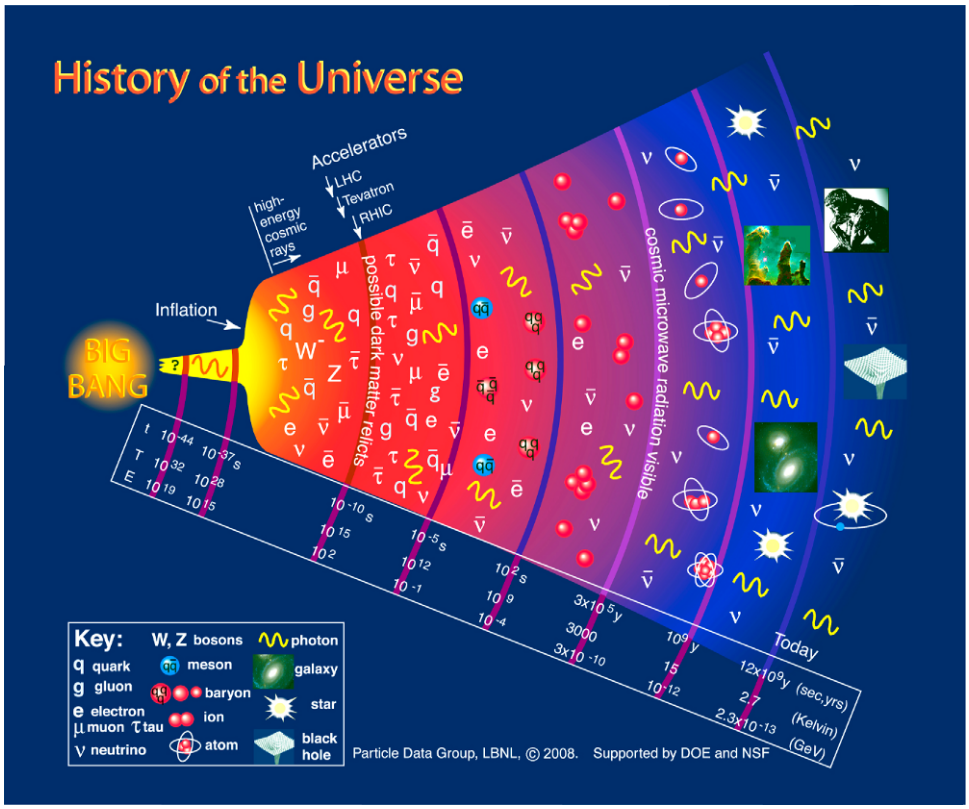

Figure 2.1: History of the Universe. Figure by Particle Data Group, LBNL.

Although the two fields are far apart, the data at hand do have commonalities. To show these commonalities, the data is presented using the same visual representation. Just as the map of the Earth is a 2D representation of a 3D spherical map so can the CMB be projected to a 2D map. The projection that is used is called a Mollweide projection, which is explained further in section 6.2. Likewise, a heavy ion collision can be presented as a 2D map in Mollweide projection. Such a map of a collision is essentially a map of point-like sources (each point is a particle) which is also known from the CMB - e.g. the map of the CMB itself at high multipoles (figure 2.3).

Most particles in a heavy ion collision hit the detector very close to the beam directions. The signal of these particles is almost independent of the azimuthal angle, ϕ, and presents itself as a band-like structure in the map. Much of the foregrounds known from CMB analysis share this band-like morphology, as does the map of pixel noise from e.g. the WMAP satellite (figure 2.2).

Furthermore, the approach presented in this thesis revolves around the exploitation of symmetries using the spherical harmonics decomposition, which is the very cornerstone of a lot of CMB research activities.

2.1 Common features

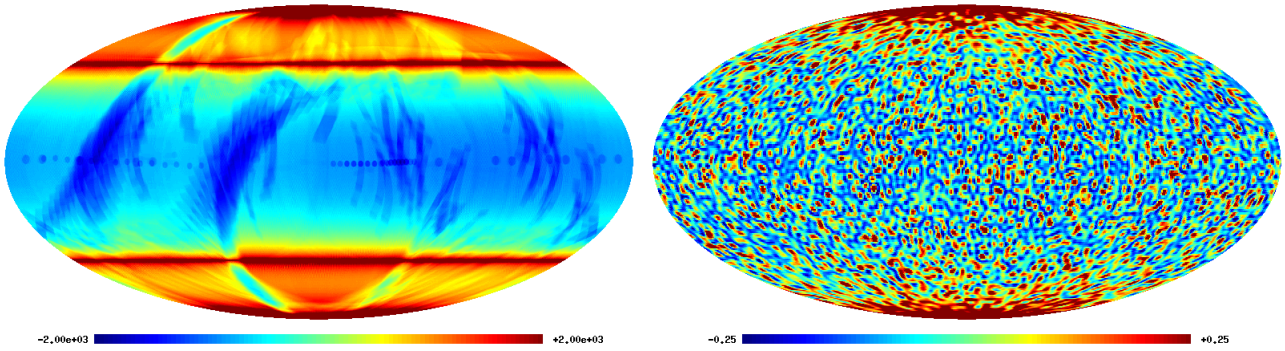

Figure 2.2: Left: The number of observations at a given point on the sky by the WMAP satellite (Mollweide projection and Ecliptic coordinates). Right: A map in Mollweide projection of a heavy ion collision.

In a perfect (fictive) experiment, all areas of the sky could be observed the same number of times. Experiments are not perfect, however, and CMB observatories such as the WMAP and Planck satellites are no exception (see section 3.2). It is therefore crucial to know exactly what the Number-of-Observations map looks like (figure 2.2). Pixels that have been observed many times will have better statistics than those who have only been observed once. Systematic errors will also be more enhanced in these areas, as will foregrounds. Figure 2.2 shows the Number-of-Observations map by the WMAP satellite in ecliptic coordinates. The relation to heavy ion physics has two sides to it. Firstly, it is something that has to be corrected for when trying to obtain a truthful map of the CMB. Likewise, heavy ion physicists have to take detector efficiency into account when analysing their data. Secondly, the signal in figure 2.2(left) is very similar to the signal seen in a heavy ion collision (figure 2.2(right)). The signal is strongest at the "poles" (top and bottom) and is (dominantly) band-like in structure - i.e. there is no azimuthal dependence.

In figure 2.3 the WMAP ILC (Internal Linear Combination) map [6] is depicted for $l = 400 - 450$. The ILC is a map of the CMB cleaned of foregrounds (as far as possible). The multipole number l is inversely proportional to angular scale - high l corresponds to small angular scales. Thus, at this range only very small structures can be seen in the map (by construction). It is seen from the figure that the map almost resembles point-like sources.

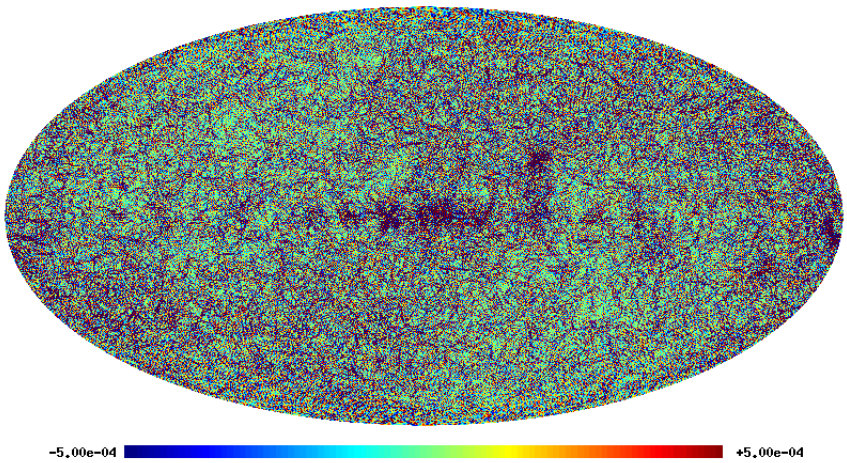

Figure 2.3: The ILC from $l = 400$ to $l = 450$ in galactic coordinates.

2.2 Subject of investigation

Using knowledge from the investigation of the morphology of the CMB, this thesis will attempt a CMB physics approach to heavy ion collision data analysis. Since the study of the morphology of a heavy ion collision is a rather broad subject, this thesis will limit itself to the study of collective flow - in particular elliptic flow. Collective flow is a phenomenon observed in heavy ion collisions of sufficiently high collision energy. The distribution of particles produced in such a collision seem to be governed by physics of the earliest stage of the collision. The difference in pressure gradients due to the initial collision geometry gives rise to an anisotropic collective flow that propagates to the final particle distribution. This causes modulations of the morphology of the signal. Flow is also a signature of the production of a QGP (see section 4.1).

The goal of this thesis is to apply CMB methods to simulated heavy ion collision data and obtain results for elliptic flow on an event-by-event basis. Such an endeavour has been motivated in this chapter, and in the following chapters the theory, background, methods and tools necessary for an analysis will be presented and developed.

Chapter 3

The CMB field

The study of the CMB is the study of light that has travelled almost unobstructed through the vast spaces of the Universe for billions of years. It is the study of photons that even today retain information about the content, morphology and structure of the Universe when it was only some hundred thousand years old. It is a secret doorway to looking back before the first stars were born and illuminated the Universe for our telescopes to see. It is the study of the Universe on the grandest of scales imaginable - the entire sky.

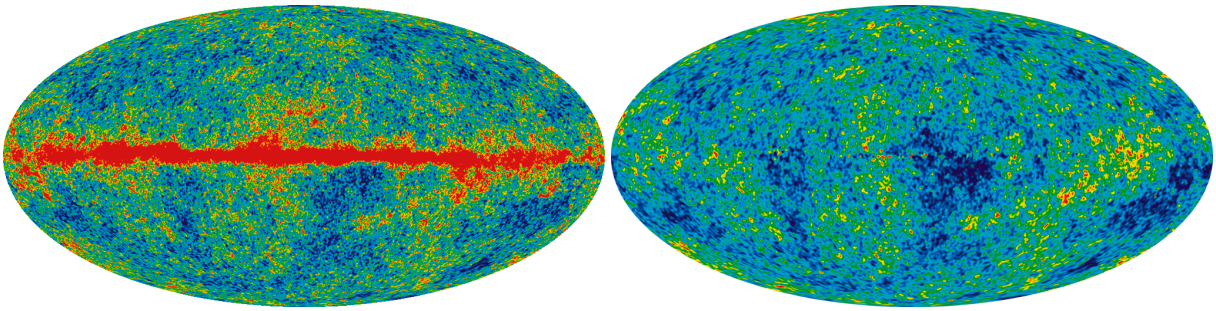

Figure 3.1: Left: The CMB in the W-band (94 GHz. Linear scale from -200 to 200 μK) from the WMAP 7 year data release. The foreground is easily seen. Right: the CMB ILC map ($l_{max} = 100$), also from the WMAP 7 year data. Both maps are in galactic coordinates, and were produced by the NASA/WMAP Science Team [7].

In order to study the CMB it has to be observed first. Due to absorption and noise in the Earths atmosphere one needs space based telescopes to obtain full-sky observations of the CMB. There have been three space based CMB observatories - only one is still operating. The first was COBE (COsmic Background Explorer)[8], which was followed by WMAP (Wilkinson Microwave Anisotropy Probe)[9]. The latest one is the Planck satellite [10]. Only data from WMAP is used in CMB studies at present (Planck data has not yet been released, and COBE data is outdated by the WMAP data). In figure 3.1 (left) a sky-map of the CMB, as observed by WMAP, is shown. It is evident that the CMB is contaminated by some sort of foreground obscuring the primordial signal, the Milky Way galactic disk being the main contributor. The WMAP ILC map (right) is cleaned of foregrounds, as far as possible [6]. The observation of

foregrounds and their removal is an important difference from between experiments.

Once observed, the CMB is analysed using various methods. When analysing the CMB it is useful to decompose it using spherical harmonics, which is a fourier transformation in spherical coordinates. The CMB is usually visually presented as a two-dimensional map in a Mollweide projection, as shown in figure 3.1.

Information on the properties of the Universe is gained from the CMB through the study of its statistical properties and morphology. The CMB can be used to constrain parameters describing the Universe such as the matter content, dark energy, the Hubble constant etc.. Various predictions for primordial and extra-galactic effects on the signal, e.g. Gaussianity (or non-Gaussianity) and the Sunyaev-Zel'dovich effect[2], can be affirmed or disproved by the data. Peculiarities of interest in the signal itself are e.g. parity asymmetry [11, 12], alignment and the quadrupole anomaly [13]. Soon, the Planck CMB data will be released, which will be substantially better than the WMAP data and also with different systematic errors. This will greatly improve CMB maps and new and exciting results are to be expected.

The rest of this chapter is organised as follows. The story of how photons in the early Universe can be seen as the Cosmic Microwave Background today is told in section 3.1, and is based on [2, ch. 1 & 2][14, 15]. Section 3.2 covers the WMAP and Planck experiments, their accomplishments (or prospective accomplishments) and shortcomings. In section 3.3 an introduction to the methods used for analysis of the CMB is presented. In section 3.4 some important results obtained from the study of the CMB until now are presented.

3.1 From the creation of the universe to the CMB - the short story

Almost every observable galaxy in the Universe share a common feature: they are all moving away from our own galaxy. But this is not all. At the same time, they are also moving away from each other at an increasing speed. There are exceptions though. The Milky Way is moving towards the Andromeda galaxy in our own local galaxy cluster (the local group), due to a decoupling from the expansion of the Universe. The galaxies themselves also consist of matter that has collapsed into structure and which thereby decoupled from the general expansion. However, the expansion of the Universe is accelerating (due to dark energy), and thus at some point the gravitational force holding both clusters of galaxies and the galaxies themselves together will not be able to counteract the expansion of the Universe. By extrapolating into the far future one may thus predict a cold, desolate Universe where everything has been torn apart.

One may also look back in time. Reversing the clock reverses the picture: everything is now moving closer together, until everything is contained in a single point - the singularity denoted as the "Big Bang". However, extrapolating this far back in time and still maintaining sensible physics has some problems. The further back in time one goes, the higher the densities and temperatures. The matter itself is squeezed together, until a point is reached where particle interactions, as described by quantum field theory, have to break down and unknown physics must rule. This happens at the Planckian scale. It is at an energy scale called the Planck Energy

[2] high energy electrons in clusters of galaxies interact with CMB photons via inverse compton scattering

defined from the Planck Time (proposed by Max Planck), which is believed to be the smallest quantum of time that can exist. Once the Planckian scale is reached it is no longer possible to do any meaningful extrapolations or assumptions. This happens at $t = 10^{-44}$s.

After this earliest time, popularly referred to as the "space-time foam", it is in fact possible to explain the underlying physics. The era succeeding the space-time foam, in the fractions of a second after the Big Bang, is called the inflationary era. During inflation the scale factor[3] of the Universe grew exponentially and thus everything expanded rapidly. Quantum fluctuations were blown up to large sizes due to this expansion and densities of any particles or photons were completely diluted.

When inflation ended the Universe was large, cool and dark - not very much like the normal hot, dense picture that is the primordial Big Bang theory. Then a reheating of the Universe occurred which is effectively the Big Bang as we know it.

After reheating the Universe was very dense and very hot, with a photon to baryon ratio of 2 million to 1. The Universe then proceeded through a period of hot plasma state, firstly as a Quark Gluon Plasma with quarks and gluons in unbound states and later in a plasma where the QGP had condensed into protons and neutrons. In this plasma photons scattered off electrons and protons, keeping matter and radiation in thermal equilibrium, and preventing any atoms from forming. Because of the high photon pressure it was not possible for ordinary matter to accumulate, but the density perturbations introduced by fluctuations during inflation provided the basis for dark matter accumulation. Dark matter is not affected by photons, and could therefore slowly but surely increase the differences in density that were already present.

The mean free path per photon was very short due to the large amount of free electrons, effectively preventing the photons from escaping to anywhere. During this period there was no longer exponential growth of the scale factor, only power law growth, as the Universe was then dominated by radiation instead of a component with constant energy density (as was the case during inflation). As the Universe expanded it cooled, and at some point the mean energy of the photons was no longer high enough to keep electrons and protons from forming neutral hydrogen. Once this started the epoch of primordial nucleosynthesis where the light elements were formed began, binding electrons to nuclei and thereby drastically lowering the abundance of free electrons. The combination of no longer being able to break apart hydrogen and the rapidly falling abundance of free electrons meant that the photons were no longer trapped but free to move through the Universe. This was the photon decoupling.

Nucleosynthesis and photon decoupling happened shortly after each other, although not exactly at the same time. Though the mean energy of the photons was too low to ionize hydrogen, there was still a large exponential tail of the distribution of photons which had very high energies. The surface of last scattering was when the photons decoupled from the matter of the Universe. It is not so much a surface as it is a layer, because photon decoupling did not happen instantaneously. Any primordial density fluctuations in the Universe would translate

[3]The scale factor of the Universe determines the expansion of space-time itself. If one imagines a grid, with two observers placed at neighbouring grid points, the expansion of the Universe is not the movement of the observers in the grid, but the expansion of the grid itself. Thus, when the Universe expands the observers find themselves to be further apart in space, and both observe the other to be moving away even though they are both standing still. It is in fact the distance between grid-points that is increasing. The scale factor describes this expansion.

into perturbations of the energy densities of the photons on the last scattering surface. Denser parts of the Universe would mean lower energy for the photons of that part (because of a higher gravitational redshift), while less dense areas would have higher energy photons. The photons have been travelling through the Universe ever since, mainly uninterrupted, and can be seen as a relic radiation today: the CMB. Thus it is possible to study primordial fluctuations and anisotropies through the CMB.

3.2 Experiments

As mentioned in the introduction of this chapter, there have been three spaced-based CMB telescopes to date. The data from the COBE satellite is no longer used as it has been outdated by the WMAP data. This section will introduce the WMAP and Planck satellites to give an overview of the more technical background for the CMB analysis and the future prospects for CMB data.

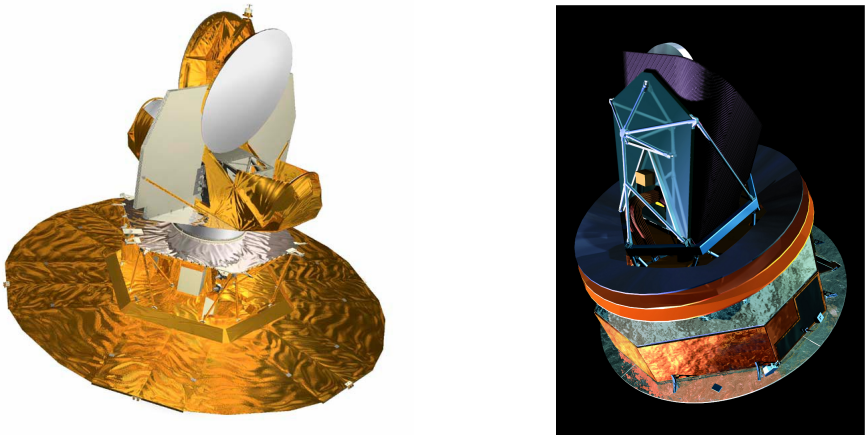

(a) The WMAP satellite.
Figure by NASA / WMAP Science Team

(b) The Planck satellite.
ESA 2002: Illustration by Medialab.

Figure 3.2: WMAP and Planck satellites.

3.2.1 WMAP

The WMAP mission was launched in 2001 and presented its first year results in 2003. The latest data, 7 year data, is from 2010 and 9 year data are expected to be released in 2012 [7]. WMAP is a space based telescope following the first space CMB-surveyor, COBE, and ended its active science observations in 2010. WMAP had the aim to investigate the CMB radiation and especially the anisotropies of the background. The science goals were to determine the parameters of the Universe to high precision, and thereby determine both content and evolution of the Universe to an unprecedented accuracy - which it has fully achieved [7]. The results for these parameters are presented in section 3.4.

While the WMAP data was a vast improvement from COBE data (see figure 3.3), the analysis of the data has presented some significant challenges. Both systematic effects (from in-

struments, satellite operation etc.) and foregrounds are difficult to completely remove from the data - even the ILC shows clear indications of residual foregrounds. Such contamination induces effects of non-cosmological origin into the CMB dataset, affecting the results of any analysis of the data.

Specifications for the WMAP instruments are listed in table 3.1.

	Frequency	Beam size (deg)	$\Delta T/T$ (μK / pixel)[4]
K	23 GHz	0.88	~ 35
Ka	33 GHz	0.66	~ 35
Q	41 GHz	0.51	~ 35
V	61 GHz	0.35	~ 35
W	94 GHz	0.22	~ 35

Table 3.1: WMAP specifications for frequency, beam size and sensitivity for each observational band [7].

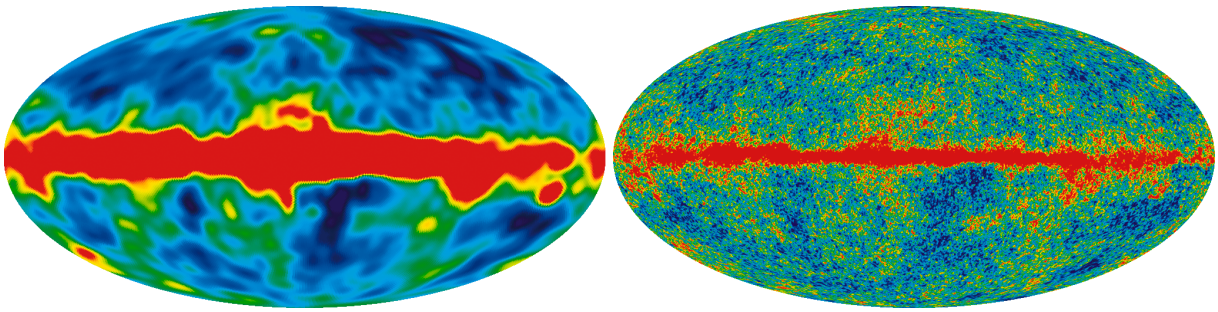

Figure 3.3: Left: The CMB at 90 GHz (Linear scale from -100 to 100 μK) from COBE. Right: The CMB in the W-band (94 GHz. Linear scale from -200 to 200 μK) from the WMAP 7 year data release. Maps produced by the NASA/WMAP Science Team [7].

3.2.2 Planck

Planck is the third generation of space based CMB telescopes. It was launched in 2009 by the European Space Agency (ESA) and is still taking data (only LFI). The scientific instruments are the Low Frequency Instrument (LFI) and High Frequency Instrument (HFI) covering the ranges 30-70 GHz (3 bands) and 100-857 GHz (6 bands) respectively. Planck represents the future of CMB science for the next years because it surpasses WMAP in both resolution, sensitivity and frequency range. This will allow testing, probing and falsifying many theories that all are in accordance with WMAP data but often in conflict with each other. Especially theories of inflation will be testable with Planck data, which will give a deep understanding of how the very beginning of our Universe took place.

Specifications for the frequency, beam width and sensitivity of Planck are listed in table 3.2, and can be compared with table 3.1 for WMAP. Note that even though the sensitivity for Planck doesn't seem to be much improved compared to WMAP this is not so. The sensitivity is listed

[4] $\Delta T/T$ is the sensitivity per pixel of 0.3 x 0.3 degrees.

as *sensitivity per pixel* - the WMAP pixel is much bigger than the Planck pixel. Thus the actual sensitivity for Planck is much higher than for WMAP.

Another advantage of Planck is that the instrumental set-up and construction of the satellite and instruments is fundamentally different from the WMAP satellite. Thus, systematic effects will be different in the two experiments and therefore easier to account for and possibly subtract from the data. The wide frequency range covers much more than just the peak of the CMB. It is also sensitive to frequency ranges were free-free emission, dust emission, synchrotron emission[5] and other foregrounds peak, allowing a much better isolation and removal of these galactic and extra-galactic foregrounds.

	Frequency	Beam-width (')	$\Delta T/T$ (μK / pixel)[6]
LFI	30 GHz	33	2
	44 GHz	24	2.7
	70 GHz	14	4.7
HFI	100 GHz	9.2	2
	143 GHz	7.1	2.2
	217 GHz	5	4.8
	353 GHz	5	14.7
	545 GHz	5	147
	857 GHz	5	6700

Table 3.2: Instrument specifics for Planck. Beam-width is in arcminutes (one degree is 60 arcminutes) at FWHM. [16].

The Planck Scientific Programme (as presented in [10] and [17]) is divided into six categories, of which three are primarily cosmological. It covers the following:

1. CMB based cosmology
2. Non-Gaussianity of the CMB
3. Secondary anisotropies
4. Extra galactic sources
5. Galactic science
6. Solar system science

The first category contains a study of the CMB anisotropies, the angular power spectrum, determination of cosmological parameters (with special focus on inflation), B-mode polarization anisotropies and gravitational lensing induced in the CMB by large scale structures. The second category concerns the possible detection of non-Gaussianity of the CMB, and the consequences

[5] Free-free emission is from free electrons scatterings off ions in the Inter Stellar Medium (ISM) of the galaxy, dust emission is from the dust in the ISM and synchrotron emission is from electrons being accelerated by the galactic magnetic field.

[6] $\Delta T/T$ is the average sensitivity per pixel achievable after two sky surveys (14 months). A pixel is a square whose side is the full width, half maximum (FWHM) extent of the beam.

hereof (see also section 3.3). It includes analysis of the bi-spectrum, testing theories of inflation, the possibility of primordial magnetic fields, studying the geometry and topology of the Universe and testing for the presence of 'defects' in the fabric of the Universe such as cosmic strings. The third category focuses on the Sunyaev-Zel'dovich effect, the ionisation history of the Universe and the dark energy equation of state. The last three categories contribute into CMB science by adding knowledge of various foregrounds (both extra galactic, galactic and from the solar system).

Planck data will be publicly available from (probably) the spring 2013.

3.3 Analysing the CMB sky

Because the CMB is an imprint of how the Universe looked at an age of $\sim 380,000$ years, it is a unique gateway to studying both the initial conditions of the Universe as well as the seeds that later became galaxies and large scale structure of the Universe. The CMB may tell us about the content of Dark Matter in the Universe, because this content has a crucial influence on the size of density perturbations at the time of decoupling. Using Monte Carlo simulations with varying values for the matter content of the Universe (and other parameters) one may try to fit the CMB data. Standard tools of the community have been developed for such simulations, e.g. CAMB [18] and Cosmo-MC [19].

The quantum fluctuations from the inflationary era that evolved into density perturbations later on are also present in the CMB. They were the seeds for the anisotropies of the CMB. In the simple inflationary models, Gaussianity of the quantum fluctuations is assumed. The morphology of the anisotropies of the CMB seems to be perfectly Gaussian in distribution, supporting these theories, but other theories propose non-Gaussian initial conditions. As was mentioned in section 3.2, WMAP data is not good enough to definitively observe non-Gaussianity but Planck data will be.

In figure 3.4 the Gaussianity of the CMB is illustrated. $H(x)$ is a probability distribution function of the CMB fluctuations, normalized to the total number of pixels. The distribution function describes the number of pixels with corresponding amplitude of fluctuations within an interval, $(x - dx, x + dx)$, starting from the minimum value of the signal and going to the maximum value. These are the fluctuations with respect to the mean value of the signal, which is why they are centered around 0. It is clear that the ILC (blue) is very close to Gaussian (red).

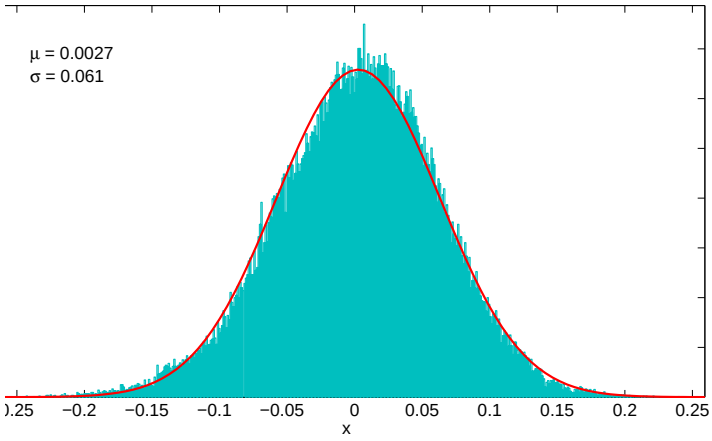

Figure 3.4: Probability distribution function of CMB fluctuations, normalized to the total number of pixels. The blue histogram is the ILC ($l_{min} = 1$, $l_{max} = 100$), and the red line is the Gaussian fit. The parameters of the fit are inserted in the plot. The binning size is $N_{bin} = 500$.

3.3.1 Spherical harmonics

When analysing the CMB, one could do the analysis of the signal on a pixel by pixel temperature basis, but it is much more convenient to quantize the signal by spherical harmonics, a three dimensional fourier transform. Both computationally and in analytical expressions it is easy to work with the spherical harmonic coefficients. A spherical harmonics decomposition of a signal, f, is given by

$$f(\theta, \phi) = \sum_{l=0} \sum_{m=-l}^{l} a_{lm} Y_{lm}(\theta, \phi). \tag{3.1}$$

Normally in CMB science it is $\Delta T/T$ and not T itself that is of interest, in which case the $l = 0$ mode (corresponding to an average over the whole sky) is omitted.

The a_{lm}'s encode all information of the signal itself, while the harmonics $Y_{lm}(\theta, \phi)$ are predefined functions on the sphere, and based on Legendre polynomials. The a_{lm}'s are complex numbers, with a real and imaginary part. It is convenient to express the coefficients as

$$a_{lm} = |a_{lm}| e^{i\Phi_{lm}}, \qquad \Phi_{lm} = \arctan\left(\frac{\Im(a_{lm})}{\Re(a_{lm})}\right). \tag{3.2}$$

l is called the multipole. For $l = 2$ there are five coefficients, but using the relationship $a_{l,-m} = a^*_{l,m}(-1)^m$ reduces this to three possible maps. In figure 3.5 the maps for these three coefficients are shown. Note that the a_{20} is completely ϕ independent.

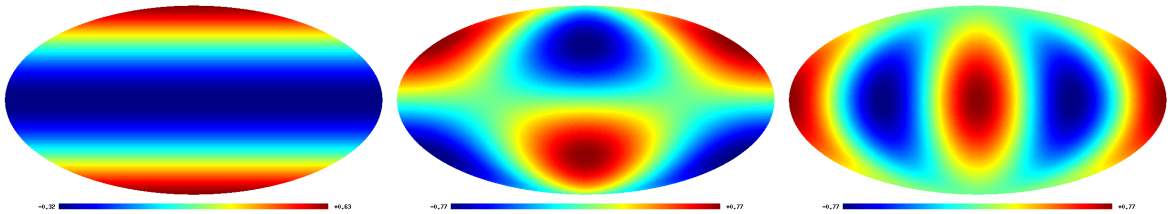

Figure 3.5: Three examples of spherical harmonics. From left to right: $(l, m) = (2, 0)$, $(l, m) = (2, 1)$ *and* $(l, m) = (2, 2)$. *The real part is set to 1 and the imaginary part to 0,* $(a_{20} = a_{21} = a_{22} = (1, 0))$.

3.3.2 The power spectrum

The power spectrum of a signal is defined as

$$C(l) = \frac{1}{2l+1} \sum_{m=-l}^{l} |a_{lm}|^2. \tag{3.3}$$

In CMB physics the power spectrum is a very powerful tool for determining cosmological parameters. The information contained in a power spectrum is a graph over the power on different scales.

3.4 CMB Results

Using statistical methods and tools optimised for the study of the CMB the best fit parameters to the theory for the Universe have been found using the WMAP data. This fit is the most accurate determination of cosmological parameters to date. These are shown in table 3.3 and constitute the ΛCDM[7] concordance model of Cosmology - the Standard Model [20, 21]. In figure 3.6 the power spectrum (multiplied by $l(l+1)/2\pi$) for the CMB is shown. The data points (WMAP) have error bars that are almost too small to see for low l. The red line is the best fit model. Markov Chain Monte Carlo formalism is used for calculating the best fit parameters.

The connection between the power spectrum and the physics of the early Universe is intricate. One connection is through the dark matter content. In the CMB power spectrum there is a very powerful peak at $l = 200$. This corresponds to the most common size of clustering of the CMB anisotropies at the time of last scattering, which in turn depends on the dark matter content. The following peaks are related to Baryonic Acoustic Oscillations in the hot plasma and help constrain dark energy [22].

[7] The ΛCDM model is a Cold Dark Matter (CDM) model including dark energy (Λ).

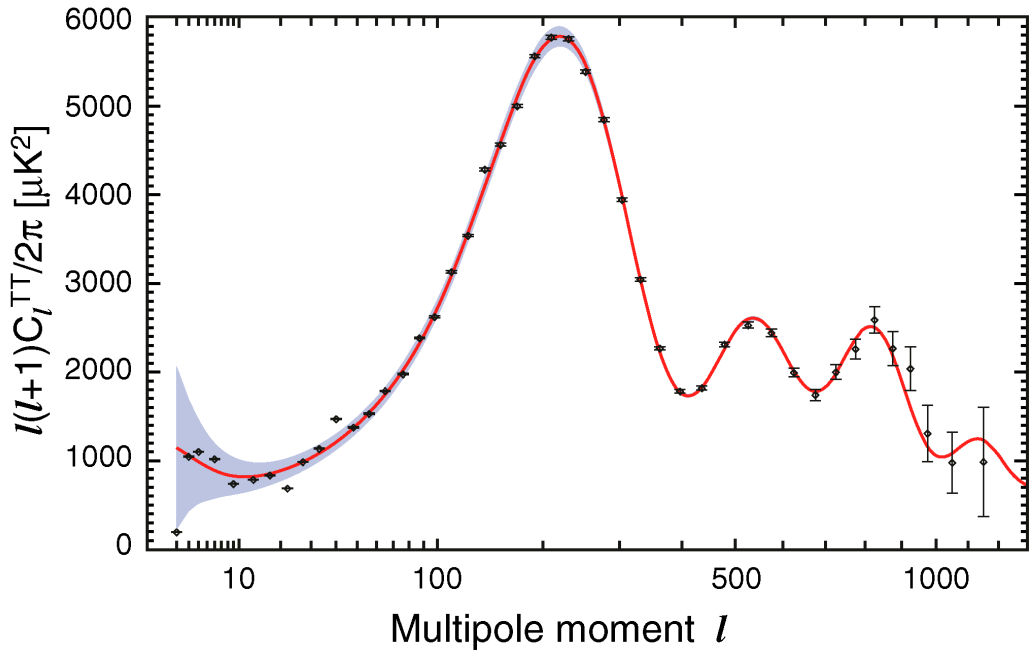

Figure 3.6: The WMAP 7 year temperature power spectrum for the CMB and the ΛCDM model best fit. The red line is the best fit of the model, and grey band is the uncertainty due to cosmic variance[9]. Figure taken from [23], by the NASA/WMAP Science Team.

In table 3.3 the best fit parameters are listed to show how high accuracy has been obtained. The parameters themselves are not used in the rest of this thesis, and are therefore only superficially explained.

Parameter	7-year Fit	5-year Fit
Fit parameters		
$10^2\Omega_b h^2$	$2.258^{+0.057}_{-0.056}$	2.273 ± 0.062
$\Omega_c h^2$	0.1109 ± 0.0056	0.1099 ± 0.0062
Ω_Λ	0.734 ± 0.029	0.742 ± 0.030
$\Delta^2_{\mathcal{R}}$	$(2.43 \pm 0.11) \times 10^{-9}$	$(2.41 \pm 0.11) \times 10^{-9}$
n_s	0.963 ± 0.014	$0.963^{+0.014}_{-0.015}$
τ	0.088 ± 0.015	0.087 ± 0.017
Derived parameters		
t_0	13.75 ± 0.13 Gyr	13.69 ± 0.13 Gyr
H_0	71.0 ± 2.5 km/s/Mpc	$71.9^{+2.6}_{-2.7}$ km/s/Mpc
σ_8	0.801 ± 0.030	0.796 ± 0.036
Ω_b	0.0449 ± 0.0028	0.0441 ± 0.0030
Ω_c	0.222 ± 0.026	0.214 ± 0.027
$z_{\rm eq}$	3196^{+134}_{-133}	3176^{+151}_{-150}
$z_{\rm reion}$	10.5 ± 1.2	11.0 ± 1.4

Table 3.3: Six-Parameter ΛCDM Fit - Models fit to WMAP data only. Table from [3]

[9]Cosmic variance is due to the fact that only one observable Universe exists, making it impossible to say whether it is statistically probable or not. Therefore, a model of the Universe (such as the ΛCDM model) can never be better than the cosmic variance [24]

$\Omega_b h^2$ and $\Omega_c h^2$ are the physical baryon and dark matter density respectively, Ω_Λ is the Dark Energy density, $\Delta^2_{\mathcal{R}}$ is the amplitude of curvature perturbations and n_s the spectral index of density perturbations ($k_0 = 0.002$ Mpc^{-1}). τ is the reionisation optical depth and A_{SZ} is the amplitude of the Sunyaev-Zel'dovich spectrum. t_0 is the age of the Universe, H_0 is the Hubble parameter ($H_0 = 100h$km/s/Mpc), z_{eq} is the redshift of matter-radiation equality and z_{reion} is the redshift of reionisation.

3.4.1 Low multipole anomalies

From the analysis of the WMAP CMB data, different issues have arisen. At the Planck group at the Discovery Center three of these have been the focus of investigations.

Firstly, the observed CMB quadrupole is very low compared to the ΛCDM model, see figure 3.6, as it cannot even be accounted for by cosmic variance [13].

Secondly, There is a peculiar alignment between the quadrupole and the octupole, commonly referred to as the 'axis of evil' [13, 25]. Two of the main principles in cosmology are the assumptions of homogeneity and isotropy on large scales. Homogeneity means there is no preferred location in the Universe and isotropy means that there is no preferred direction. This is to be expected if the origin of structure in the universe is random Gaussian fluctuations during the inflationary period. Therefore an alignment in quadrupole and octupole - indicating a preferred direction - is in contradiction to strong basic cosmological assumptions.

Thirdly, parity asymmetry is observed in the Universe. Parity symmetry is if the signal in one direction in the sky and the signal in the exact opposite direction is the same ($S(\hat{\mathbf{n}}) = S(-\hat{\mathbf{n}})$) and parity asymmetry is if the signal is $S(\hat{\mathbf{n}}) = -S(-\hat{\mathbf{n}})$. The Universe is expected to show neither parity symmetry nor parity asymmetry, due to causality[10]. Instead, the signal should show random behaviour [11, 12]. In figure 3.7 the parity asymmetry is documented. P^+/P^- is defined from

$$P^+ = \sum_{l=2}^{l_{max}} \frac{1}{2}(1 + (-1)^l) l(l+1)/2\pi C_l,$$
$$P^- = \sum_{l=2}^{l_{max}} \frac{1}{2}(1 - (-1)^l) l(l+1)/2\pi C_l. \tag{3.4}$$

$P^+/P^- > 1$ means parity symmetry and $P^+/P^- < 1$ means parity asymmetry.

[10] It is hard to avoid that the Universe should show even parity preference on large scales.

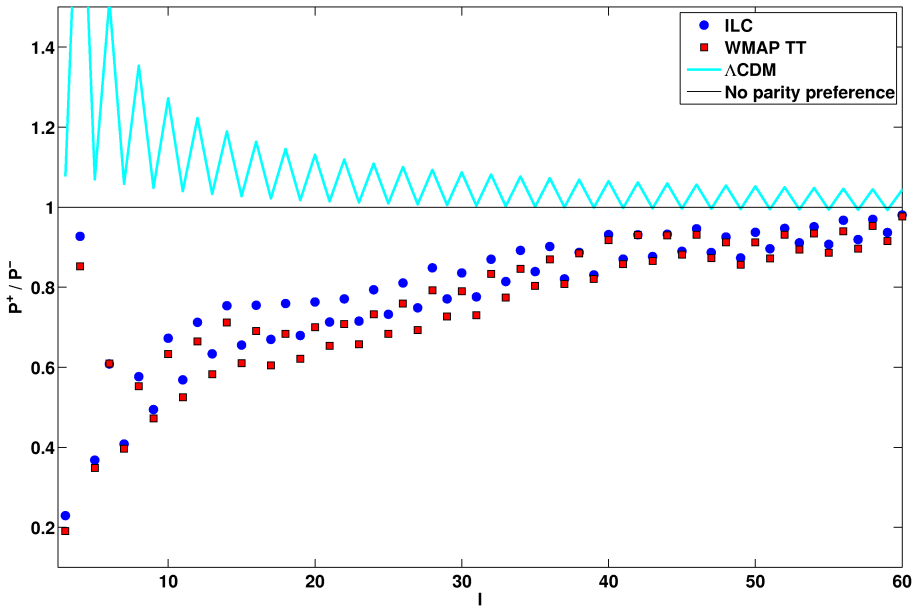

Figure 3.7: P^+/P^- for the ILC (blue dots), the WMAP Temperature power spectrum (red squares) and the ΛCDM model (blue line). If $P^+/P^- = 1$ the power in even (symmetric) and odd (asymmetric) multipoles is the same, and there is neither parity asymmetry nor asymmetry.

It is expected that these issues will be resolved with the coming release of Planck CMB data. Either by being proven to be effects caused by non-cosmological contributions in the signal (noise, foregrounds, systematic effects) or by proving to be true features of the signal and thus creating the need for new physics to explain them.

The connection to heavy ion physics is through symmetries. Symmetry is a critical issue for the CMB (e.g. no preference for even or odd modes in the parity and no preferred direction in the Universe is expected). For heavy ion physics, the collisions of highly relativistic heavy ions express a very high degree of symmetry. This commonality in symmetry will be exploited in the next chapters.

Chapter 4

Heavy ion physics

With the CMB side of the story covered it is time to look at the field of application - heavy ion physics.

Heavy ion physics is the study of matter under the extreme conditions created in collisions of highly relativistic heavy ions. Such conditions are created by colliding e.g. Au (gold) or Pb (lead) ions in particle accelerators such as RHIC (Relativistic Heavy Ion Collider) at the Brookhaven National Laboratory or the LHC (Large Hadron Collider) at CERN (European Organization for Nuclear Research).

The particles produced in heavy ion collisions are measured and various features of the collision may be studied. E.g. particle species, the momentum distribution, the multiplicity and the morphology of the particle distribution. The morphology is of particular interest because it carries information about very fundamental physics on the quark level [26]. The study of this morphology is also the study of the initial collision geometry, which will be explained in more detail in section 4.2.

To describe the particles produced in a heavy ion collision various parameters are important. Each particle has a transverse momentum (transverse to the beam axis), defined by $p_t \equiv \sqrt{p_x^2 + p_y^2}$ (see definition of $\boldsymbol{x}$ and $\boldsymbol{y}$ in figure 4.1). The particles also have a momentum in the beam direction $\boldsymbol{z}$, p_z. This goes into the definition of rapidity, y (which should not be confused with the spatial coordinate), $y \equiv ln\frac{1}{2}\left(\frac{E+p_z}{E-p_z}\right)$ where E is the energy of the particle [27]. In contrast to p_z the merit of rapidity is that it is Lorentz invariant.

Determining momentum requires knowledge of both mass and velocity, as does determining the rapidity. Since the mass of a particle is not always known in an experiment it is convenient to define a pseudorapidity, η,

$$\eta = -\ln\left(\tan\left(\frac{\theta}{2}\right)\right). \tag{4.1}$$

Here θ describes the angle between the momentum vector of the outcoming particles and the beam axis, z. For $m \ll p$, $y \to \eta$.

Using a fourier expansion of the azimuthal dependence of the particle distribution in re-

spect to the reaction plane, one obtains [28].

$$E\frac{d^3N}{d^3p} = \frac{1}{2\pi}\frac{d^2N}{p_t dp_t dy}\left(1 + 2\sum_{n=1}^{\infty} v_n cos(n[\phi - \Psi_n])\right), \tag{4.2}$$

The coefficient of expansion describe the different orders of anisotropic collective flow, v_n, as will be explained in section 4.2.

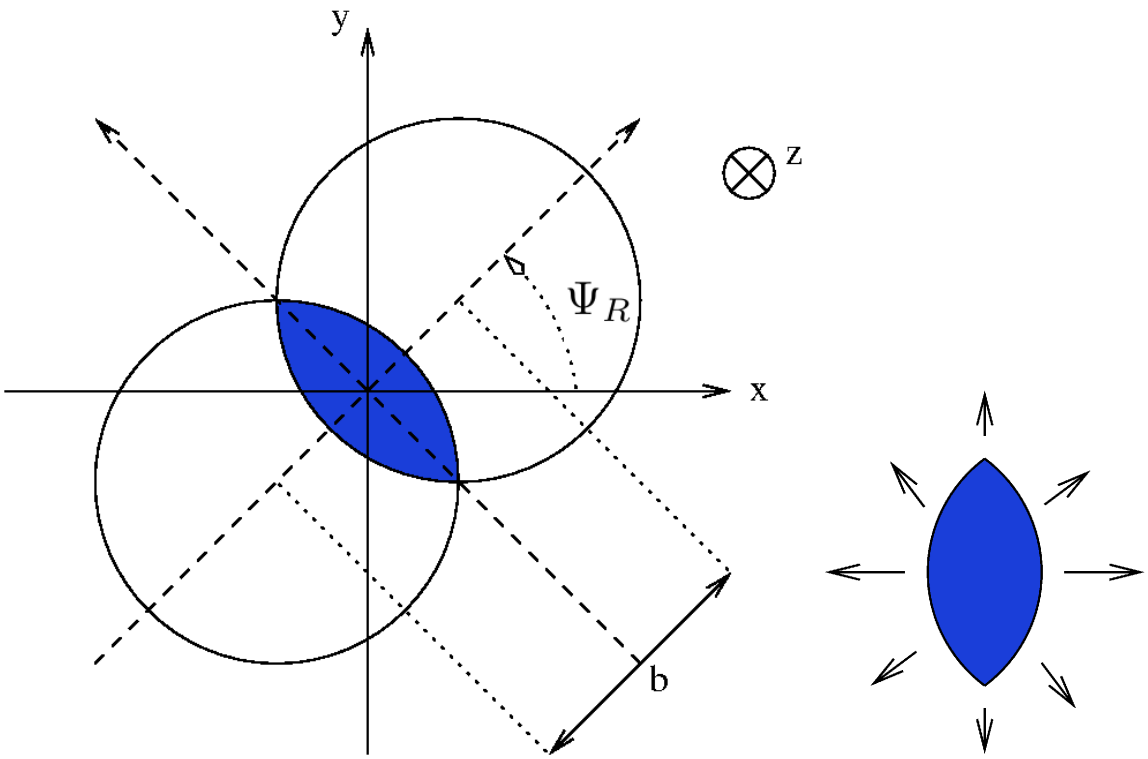

Figure 4.1: The two overlapping circles are the two colliding nuclei. The shaded area is the participant region, which is where the nuclei actually collide. ***b*** *is the impact parameter.* ***z*** *is the beam axis,* ***x*** *and* ***y*** *define the transverse plane. The reaction plane angle, Ψ_R, is also defined. Lower right corner: The almond shaped region of interaction.*

In a collision, the amount of produced particles is called the multiplicity. Two other parameters of importance is the impact parameter and the closely related centrality [29]. The impact parameter **b** in figure 4.1 is defined as the vector from the center of one colliding nucleus to the other. The impact parameter itself is not observable, instead one uses centrality. One is interested in how central a collision is, because the physical observables depend on the centrality of the collision. E.g. a very central collision produces a high multiplicity whereas a very peripheral collision results in very low multiplicity, because most of the nucleons in the two nuclei do not participate in the collision. It is exactly the dependence on multiplicity that is used to determine the centrality [30].

4.1 Quark Gluon Plasma

QGP is a phase of de-confined quarks and gluons at high energy densities of order 1 GeV fm^{-3} (the energy density inside a heavy nucleus is ~ 6 times smaller than this) [27, Ch. 1]. The very early Universe had such high energy densities before it expanded and cooled, causing the QGP to do a phase transition to bound states - hadrons. Since the early Universe, quarks and gluons have been confined to hadrons[11]. In heavy ion collisions one can reverse the order and make a transition from bound state quarks and gluons to a QGP, if the collision energy is high enough. However, one cannot observe the QGP directly because it is so short-lived - the plasma cools fast, and the quarks and gluons are no longer free but combine into hadrons that are subsequently detected by the detector. Different particle production mechanisms and effects are predicted for a collision where a QGP has been produced than for a collision where it has not [31, Ch. 7][32]. The QGP can be either strongly interacting (sQGP), in which case an effect is the presence of collective anisotropic flow, or weakly interacting. Collective flow is a hydrodynamical feature, and can only be produced in a collision if a sQGP phase is created and has had time to reach local equilibrium [26, 27].

4.2 Flow

Due to the relativist speed of the ions they are Lorentz contracted, and thus appear pancake-like in the laboratory frame of reference. One can project the collision geometry to a two-dimensional picture as illustrated in figure 4.1. Here the overlap between the two nuclei is approximately almond-shaped, except for very central collisions [33, 34]. The almond-shaped region is spatially very anisotropic and gives rise to different pressure gradients along the major and minor axis. These propagate to an anisotropy in the azimuthal particle yield. The collision itself creates a QGP state, which has been found to behave like a fluid [35, 36]. Thus, the propagation of particles due to different pressure gradients does so through a fluid dynamical flow [33, 34, 37, 38]. Recent experimental results indicate that anisotropic collective flow is sensitive to the viscosity of the system [4, 5].

For the particle distribution collective flow is a modulation in ϕ. In cylindrical coordinates the signal from a collision (Eq.(4.2)) can be represented by:

$$S(z,\phi) = R(z,\phi)\left(1 + 2\sum_{n\geq 1} v_n \cos(n[\phi - \Psi_n])\right), \tag{4.3}$$

where $R(z,\phi)$ is a 'background' signal without any collective flow, and the v_n describe the amplitude of collective flow of order n. Ψ_n is the event plane angle.

The almond-shaped region of interaction, as shown in figure 4.1, is well fitted by an elliptic shape. The anisotropic flow connected with this shape of the matter is called elliptic flow (v_2). This picture is simplified, however. The nuclei are composed of protons and neutrons, and the

[11] There are speculations that the extreme densities in neutron stars may allow for free quarks and gluons, but this has yet to be observed.

participating nucleons are randomly distributed inside the nucleus. These perturbations are the cause of higher order flow moments, $v_3, v_4, ..$, etc., which give rise to other shapes than just an ellipse. This has also been seen recently experimentally [39–44].

The reaction plane angle, Ψ_R, is defined from the reaction plane. The reaction plane is defined to be the plane spanned by the impact parameter vector **b** and the z axis (see figure 4.1). The event plane angle, Ψ_n, is related to the planes of symmetry of the collision, n. The eccentricity of the ellipse (almond-shape) in figure 4.1 depends on how much the two nuclei overlap, and its orientation depends on how their centers are located with respect to each other. The actual elliptical shape of the participating nucleons may be shifted slightly in respect to the major axis of the 'perfect' ellipse, because of the random distribution of the nucleons inside the nuclei. The angle of this actual elliptical shape is the one that can be measured experimentally as Ψ_2. Higher order flow moments result from the shape of the initial geometry of the collision being different from that of an elliptic shape - e.g. a triangular shape. Such flow, here v_3, would give rise to event plane angles Ψ_3 which are totally uncorrelated with Ψ_2. By definition Ψ_2 is closely related to Ψ_R.

The standard heavy ion analyses utilise two- and multi-particle correlation methods to extract information about collective flow from heavy ion collisions [33, 34]. However, these methods suffer from problems with separation of components, a problem also known in CMB physics. A heavy ion collision does not only produce collective flow, but also dynamical features[12] such as jets, resonance decays etc.. The approach is then to either clean the signal of anything but collective flow in order to study that particular effect, or to remove collective flow effectively from the signal in order to study e.g. jets without bias [1].

4.3 The ALICE experiment

This thesis deals with simulations of heavy ion collisions at energies obtainable with the LHC at CERN. Since the natural extension of the analysis of simulated data is to real observational data, a word on the LHC and its experiments is appropriate. The methods can also be applied to other experiments that can obtain multiplicities comparable to those observed at the LHC.

The LHC is a huge circular collider with a circumference of 27 km. It was designed to collide beams of protons or lead ions, and in 2011 it has been doing so at energies of up to 7 TeV/nucleon for protons and 2.76 TeV/nucleon for lead ions. The beams are brought to collide at the sites of the experiments [45].

There are four major experiments at the LHC. ATLAS (A Toroidal LHC ApparatuS) and CMS (Compact Muon Solenoid) which are both looking for new physics - e.g. the Higgs - in proton-proton collisions. LHCb (Large Hadron Collider beauty) looking for - among other things - the reason for the universal matter-antimatter inequality and lastly ALICE, a general purpose detector optimized for observing heavy ion collisions, looking at e.g. glass-colour condensate, QGP etc. in heavy ion collisions [45].

[12] Dynamical features are correlations of "few" particles whereas collective features involve correlations of many (or all) particles in a collision.

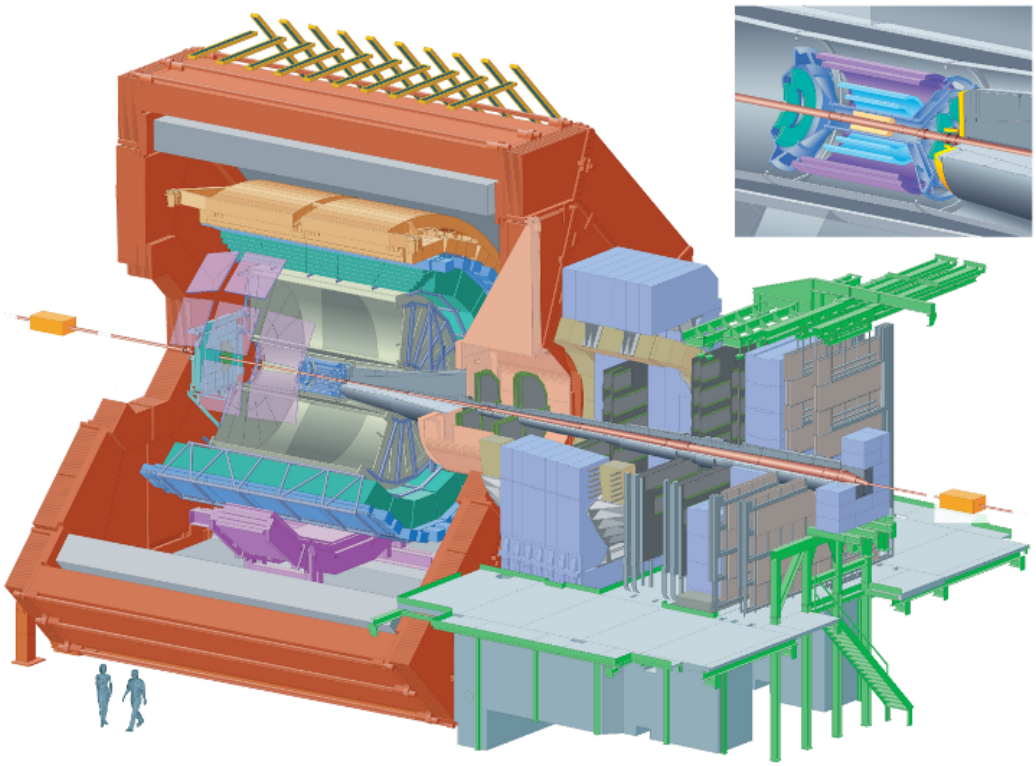

Figure 4.2: The ALICE experiment. Top right corner shows the inner detectors, where the collision takes place. Figure by the ALICE collaboration.

Part II

Methods

Chapter 5

Mathematical tools

Now the theoretical basis and background has been laid out for both the CMB field - the theoretical basis for this thesis - and the heavy ion field - the data to be analysed. This chapter will develop the mathematical methods, tools and derivations to be used in the analysis of heavy ion data. The next chapter will cover the CMB tools for the processing of data and how to deal with the heavy ion signal in a CMB framework. The methods and tools of this part will be implemented in the analysis in part III.

The aim of this chapter is a mathematical method for determining the amplitude of elliptic flow in a heavy ion collision, and the determination of the event plane angle, Ψ_n. The chapter starts with a word on symmetries of a signal. This is followed by a decomposition of a heavy ion signal into spherical harmonics in section 5.2. In section 5.3 a direct determination of flow through spherical harmonic coefficients is investigated.

5.1 Using symmetries

Using the spherical harmonics representation introduced in section 3.3.1 one can investigate the symmetries and anti-symmetries of a signal.

For any spherical signal $s(\hat{\mathbf{n}})$ with unit vector $\hat{\mathbf{n}} = (\theta, \phi)$, one can define its symmetric, $s^+(\hat{\mathbf{n}})$, and antisymmetric, $s^-(\hat{\mathbf{n}})$, parts

$$s(\hat{\mathbf{n}}) = s^+(\hat{\mathbf{n}}) + s^-(\hat{\mathbf{n}}) \tag{5.1}$$

To define these components of the signal, note that the symmetric part is expected to be zero for all odd l, and the antisymmetric part is expected to be zero for all even l. Furthermore $s^+(\hat{\mathbf{n}})$ and $s^-(\hat{\mathbf{n}})$ should be normalized, to give $s(\hat{\mathbf{n}})$ when added. The components are described by [46]

$$s^+(\hat{\mathbf{n}}) = \frac{s(\hat{\mathbf{n}}) + s(-\hat{\mathbf{n}})}{2} = \sum_l \sum_{m=-l}^{l} a_{lm} Y_{lm}(\hat{\mathbf{n}}) \cos^2\left(\frac{\pi l}{2}\right) \tag{5.2}$$

$$s^-(\hat{\mathbf{n}}) = \frac{s(\hat{\mathbf{n}}) - s(-\hat{\mathbf{n}})}{2} = \sum_l \sum_{m=-l}^{l} a_{lm} Y_{lm}(\hat{\mathbf{n}}) \sin^2\left(\frac{\pi l}{2}\right) \tag{5.3}$$

The distribution of particles produced in a heavy ion collision shows a very high degree of symmetry. Flow is also a very symmetric modulation of the signal. Thus, it should show up very strongly in the symmetric part - i.e. even multipoles - of the signal. In a power spectrum (see Eq.(3.3)), symmetric particle distributions will express themselves in a strong preference of even multipoles over odd ones.

5.2 Decomposition of the signal

A fourier transform is a representation of a signal through a superposition of sinusoidal functions. In one dimension the fourier transform of the function $f(x)$ is defined as

$$\tilde{f}(k) = C \int_{-\infty}^{\infty} f(x) e^{-ikx} dx, \tag{5.4}$$

where C is a constant [47]. One can also do the fourier transform discretely as a sum instead of an integral.

For a spherical signal in three dimensions one should use spherical harmonics to do the fourier transformation. These were introduced in section 3.3.1. The signal is then represented by coefficients and harmonics, where the coefficients encode all the information of the original signal.

The decomposition of the signal into fourier (spherical harmonics) coefficients is useful, because one can do analytical manipulations on the coefficients easily. It is also computationally less costly to do calculations in fourier space than in pixel space. This section will derive the equations for the decomposed heavy ion signal. This will be used for the derivation of equations for determination of flow in section 5.3.

Tools for CMB analysis have been developed for decomposing a spherical signal into spherical harmonics, as will be described in chapter 6.

5.2.1 Spherical harmonics decomposition

The signal in Eq.(4.3) in spherical coordinates is given by

$$S(\theta, \phi) = R(\theta, \phi) \left(1 + 2 \sum_{n \geq 1} v_n \cos(n[\phi - \Psi_n]) \right). \tag{5.5}$$

The fourier decomposition is now done by using spherical harmonics,

$$\begin{aligned} S(\theta, \phi) &= \sum_{l,m} a_{lm} Y_{lm}(\theta, \phi) \\ R(\theta, \phi) &= \sum_{l,m} c_{lm} Y_{lm}(\theta, \phi) \\ \int_{\Omega} S(\theta, \phi) Y^*_{l'm'} d\Omega &= a_{lm} \delta_{l',l} \delta_{m',m}, \end{aligned} \tag{5.6}$$

and by using that

$$\cos(nx) = \frac{e^{inx} + e^{-inx}}{2}. \tag{5.7}$$

Substituting into Eq.(5.5) gives

$$\begin{aligned}\int_\Omega S(\theta,\phi)Y^*_{l'm'}d\Omega &= \int_\Omega R(\theta,\phi)Y^*_{l'm'}d\Omega + \sum_{n\geq 1} v_n \int_\Omega R(\theta,\phi)e^{in(\phi-\Psi_n)}Y^*_{l'm'}(\theta,\phi)d\Omega \\ &\quad + \sum_{n\geq 1} v_n \int_\Omega R(\theta,\phi)e^{-in(\phi-\Psi_n)}Y^*_{l'm'}(\theta,\phi)d\Omega. \end{aligned} \tag{5.8}$$

Using the orthogonality of Y_{lm}'s, one can do the integral and obtain the coefficients,

$$\begin{aligned} a_{lm} &= c_{lm} + \sum_{n\geq 1} v_n e^{-in\Psi_n} \int_\Omega \sum_{l,m} c_{lm}Y_{lm}(\theta,\phi)Y^*_{l'm'}(\theta,\phi)e^{in\phi}d\Omega \\ &\quad + \sum_{n\geq 1} v_n e^{in\Psi_n} \int_\Omega \sum_{l,m} c_{lm}Y_{lm}(\theta,\phi)Y^*_{l'm'}(\theta,\phi)e^{-in\phi}d\Omega \\ &= c_{lm} + \sum_{n\geq 1} v_n \left(c_{l,m+n}e^{-in\Psi_n} + c_{l,m-n}e^{in\Psi_n}\right). \end{aligned} \tag{5.9}$$

Note that a_{lm} is the observed signal, whereas c_{lm} is the constrained random signal without any modulations. In an event only a_{lm} is available, and all knowledge on v_n and Ψ_n must be extracted from it.

See appendix A for more details on the above derivations, as well as a cylindrical decomposition (the coordinate system of the detector) for comparison.

5.3 Determining the flow

Chapter 4 motivated the importance of flow in heavy ion collisions. This section will use a CMB approach to formulate mathematical tools for the investigation of flow - both elliptic and higher orders.

This section discusses the dominance of the components of the signal, and a way of effectively removing 'background' signal without removing the flow signal. Also, general equations will be derived for even and odd flow moments, as well as a derivation of a direct way of calculating the amplitude of elliptic flow in an event.

5.3.1 A very dominant background

When two nuclei collide in a heavy ion collision they are travelling at very high energies along the beam axis. The collision leads to a very high concentration of outcoming particles along the beam axis. If one sees the particle distribution in a spherical representation where the z-coordinate is replaced by θ (see section 6.1), this would mean a very powerful signal around the polar caps and a weaker contribution at the equator. In the spherical harmonics decomposition of such a signal, the $a_{l,m=0}$ mode would be very dominant, especially at low multipoles, because

the $m = 0$ mode is constant in ϕ - it therefore fits very well with the symmetry of a collision (see figure 3.5).

In the study of finer structures or modulations, the strong signal from particles in the beam direction can be treated as a background. Omitting all $m = 0$ modes in a spherical harmonic reconstruction of the signal removes much of such a background. A modulation in ϕ, such as flow, should not be affected by the removal of the $m = 0$ modes.

A method for ensuring that removal of $m = 0$ removes unwanted background and isolates information on the morphology of the fluctuations of the event, is taking a look at the power spectrum, C^T,

$$C^T(l) = \mathcal{C}(l) + D(l) = \frac{1}{2l+1}\left(|a_{l,m=0}|^2 + 2\sum_{m=1}^{l}|a_{lm}|^2\right). \tag{5.10}$$

Here the total power spectrum is split into $\mathcal{C}(l)$ which contains the most azimuthally symmetric part of the signal, contained in all $m = 0$ modes, and $D(l)$ which contains information on all $|m| > 0$ modes. An example of such a power spectrum is presented in figure 5.1, left. It indicates that the two components have very different properties.

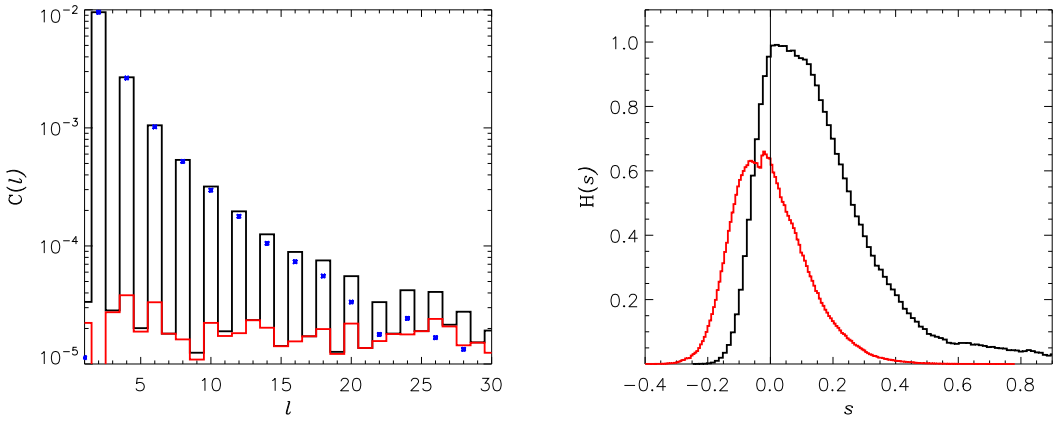

Figure 5.1: Left: power spectrum of a heavy ion event. The black line is the total power spectrum, blue dots is $\mathcal{C}(l)$ and the red line is $D(l)$. Right: the normalised distribution function, H(s), of the amplitude of fluctuations. The black line is for the total signal, and the red line is for $m = 0$ removed. Figure from [1].

If a collision produced a totally symmetric signal around $\theta = \pi$, all odd-components of the power spectrum would vanish, following Eq.(5.3). Even though a collision does not produce perfect symmetry, the strong suppression of odd-modes in C^T in figure 5.1 shows that it is remarkably symmetric. The total signal is of course always a positive count of particles, but when the mean signal is subtracted the resulting signal is both positive and negative with respect to the mean. The strong presence of particles in the beam direction causes areas of strongly positive fluctuations with respect to the mean. The removal of this "background" should give a symmetric distribution of fluctuation-amplitudes around the mean. This is exactly what is shown in figure 5.1 right. $H(s)$ is the probability distribution function, normalised to the total

amount of pixels, $N_{tot} \propto 8l_{max}^2$ [13]. The number of bins is 200. s is the signal, which is the amplitude of fluctuations after the mean signal has been removed. It is clear that the removal of the $m = 0$ mode converts the signal from a strong preference for positive signal to an almost Gaussian distribution around zero, confirming the successful subtraction of unwanted background [1].

5.3.2 v_n modulation for even n

In this section a mathematical expression for isolating the amplitude of v_n, for even n, in an event is sought.

The final equation of section 5.2.1 is revisited,

$$a_{lm} = c_{lm} + \sum_{n\geq 1} v_n \left(c_{l,m+n} e^{-in\Psi_n} + c_{l,m-n} e^{in\Psi_n} \right). \tag{5.11}$$

The most powerful component of the signal is the $m = 0$ mode of the background - $c_{l,0}$ - according to section 5.3.1. Clearly $a_{l,0}$ is then dominated by $c_{l,0}$,

$$\begin{aligned} a_{l,0} &= c_{l,0} + \sum_n v_n \left(c_{l,n} e^{-in\Psi_n} + c_{l,-n} e^{in\Psi_n} \right) \Leftrightarrow \\ |a_{l,0}| &= |c_{l,0}| + \sum_n v_n |c_{l,n}| 2\cos(\Phi_{c_{l,n}} - n\Psi_n) \\ &\approx |c_{l,0}|. \end{aligned} \tag{5.12}$$

To obtain this result some mathematical relationships for spherical harmonics and their coefficients are used. Firstly $a_{lm}|_{|m|>l} = 0$, which removes all coefficients where $|m|$ becomes bigger than l, while $a_{l,-m} = a_{l,m}^*(-1)^m$ eliminates a_{lm}'s with a negative m-value. Secondly, the fact that one can split the coefficient into a real part and an imaginary part (Eq.(3.2)). If $m = 0$ the phase is zero, i.e. $\Phi_{c_{l,0}} = 0$, because the imaginary part for a coefficient with $m = 0$ is always zero. The last step uses that we can assume $|c_{l,0}| \gg |c_{l,m\neq 0}|$ (as argued in section 5.3.1).

$c_{l,0}$ is also in resonance with $a_{l,m\neq 0}$ modes. I.e. there are $a_{l,m\neq 0}$ modes that are coupled to $c_{l,0}$ because of the mixing of modes in Eq.(5.11) ($m \pm n$ instead of m). From Eq.(5.11) it is clear that $a_{l,m\neq 0}$ is maximal if $m = n$, because the last term in the brackets then becomes $c_{l,0}$. For $n = even$ this is $a_{22}, a_{42}, a_{44}, a_{62}, ...$, because $l = even$ dominates completely over odd l, as argued in section 5.1.

For $l = 2$ the only resonance with $c_{2,0}$ is $a_{2,2}$ through v_2. For $l = 4$ both $a_{4,2}$ (through v_2) and $a_{4,4}$ (through v_4) are in resonance with $c_{4,0}$. This motivates the more general formula, for a given n

$$\begin{aligned} a_{n,n} &= c_{n,n} + v_n c_{n,0} e^{in\Psi_n} \Leftrightarrow \\ |a_{n,n}| &= |c_{n,n}| e^{i(\Phi_{c_{n,n}} - \Phi_{a_{n,n}})} + v_n |c_{n,0}| e^{-i(\Phi_{a_{n,n}} - n\Psi_n)}. \end{aligned} \tag{5.13}$$

[13] $N_{tot} = N_\theta \cdot N_\phi = 8l_{max}^2 + 8l_{max} + 2 \propto 8l_{max}^2$. N_θ is the number of bins in the θ direction, and N_ϕ the number of bins in the ϕ direction. The relationship with l_{max} is $N_\theta \geq 2l_{max} + 1$ and $N_\phi = 2N_\theta$.

Provided that the amplitude of the flow is strong enough that the assumption $v_n|c_{n,0}| \gg |c_{n,n}|$ is valid, v_n can be isolated using Eq.(5.12) and Eq.(5.13),

$$v_n \simeq \frac{|a_{n,n}|}{|a_{n,0}|}, \qquad n\Psi_n = \Phi_{a_{n,n}}. \tag{5.14}$$

For v_2 this is easily shown to be true,

$$\begin{aligned} a_{2,2} &= c_{2,2} + v_1 c_{2,1} e^{i\Psi_1} + v_2 c_{2,0} e^{i2\Psi_2} + v_3 c_{2,1}^* e^{i3\Psi_3}(-1) + v_4 c_{2,2}^* e^{i4\Psi_4} \Rightarrow \\ |a_{2,2}| &\approx v_2 |c_{2,0}| e^{-i(\Phi_{a_{2,2}} - 2\Psi_2)}. \end{aligned} \tag{5.15}$$

Thus, only the $n = 2$ flow component is contributing to the $a_{2,2}$ coefficient which makes it a good estimator for the amplitude of the elliptic flow. By dividing $|a_{2,2}|$ by $|a_{2,0}|$ (in accordance with Eq.(5.14)), v_2 can be found

$$\begin{aligned} \frac{|a_{2,2}|}{|a_{2,0}|} &\approx \frac{v_2 e^{i2\Psi_2}|c_{2,0}|}{|c_{2,0}|e^{i\Phi_{a_{2,2}}}} \\ &= v_2 e^{-i(\Phi_{a_{2,2}} - 2\Psi_2)} \\ &= v_2, \qquad 2\Psi_2 = \Phi_{a_{2,2}}. \end{aligned} \tag{5.16}$$

This gives a direct analytical result for the elliptic flow from a single event decomposed into spherical harmonics, as well as a result for the event plane angle for elliptic flow, Ψ_2.

5.3.3 v_n modulation for odd n

As mentioned in section 4.2 higher order flow-moments are also seen in the data, including flow-moments where $n = odd$. Although Eq.(5.16) is in principle also valid for odd n it is not very useful because $l = odd$ is very suppressed in the signal.

By the same arguments as for the even moments, $a_{l,m}$ is in resonance with $c_{l,0}$ through the odd n flow moments for $a_{2,1}$ (v_1), $a_{4,1}$ (v_1) and $a_{4,3}$ (v_3), etc. The formula for $n = odd$ flow is simply

$$\begin{aligned} a_{n+1,n} &= c_{n+1,n} + v_n c_{n+1,0} e^{in\Psi_n} \Leftrightarrow \\ |a_{n+1,n}| &= |c_{n+1,n}| + v_n |c_{n+1,0}| e^{-i(\Phi_{a_{n+1,n}} - n\Psi_n)}. \end{aligned} \tag{5.17}$$

This gives the general formula

$$v_n \simeq \frac{|a_{n+1,n}|}{|a_{n+1,0}|} \qquad n\Psi_n = \Phi_{a_{n+1,n}}, \tag{5.18}$$

for $n = odd$.

5.3.4 Uncertainties of the calculation

Because this approach on determining the amplitude of elliptic flow and Ψ_n is aimed at an event-by-event analysis (it can of course also be used on an ensemble of events), one needs a measure for the uncertainty of the resultant v_2. Since there is no ensemble of events to make a statistical uncertainty by, another way of quantifying the uncertainty is needed. For this a_{21} is examined. Because the signal is Gaussian (as shown in section 5.3.1) the probability density functions for a_{lm}'s with same l values are the equivalent (except for $m = 0$) if there are no modulations, i.e. no flow [24, Ch. 8.5]. Since v_2 does not contribute to a_{21} it is a good coefficient to compare a_{22} to, since they share statistical properties.

$$\begin{aligned} a_{2,1} &= c_{2,1} + \sum_{n\geq 1} v_n \left(c_{2,1+n} e^{-in\Psi_n} + c_{2,1-n} e^{in\Psi_n} \right) \\ &= c_{2,1} + v_1(c_{2,2} e^{-i\Psi_n} + c_{2,0} e^{i\Psi_n}) + v_2 c_{2,-1} e^{i2\Psi_n} + v_3 c_{2,-2} e^{i3\Psi_n} \\ &\approx v_1 c_{2,0} e^{i\Psi_n} \Leftrightarrow \\ |a_{2,1}| e^{i\Phi_{a_{2,1}}} &\approx v_1 e^{i\Psi_n} |c_{2,0}|. \end{aligned} \tag{5.19}$$

Thus, a_{21} has no contribution from $n > 1$ flow, provided that $v_1|c_{20}|$ is the dominant part of the signal. $\frac{|a_{2,1}|}{|a_{2,0}|}$ can be used as an order of magnitude indication of the uncertainty on $\frac{|a_{2,2}|}{|a_{2,0}|}$.

Note that the approach for determining the flow is limited by the level of statistical noise in the data. For a Gaussian signal this level is determined by $\frac{dN}{N} \approx \frac{1}{\sqrt{N}}$ [48, Ch. 4], where N is the multiplicity, and thus

$$\frac{1}{\sqrt{N}} \leq v_n. \tag{5.20}$$

For a $v_2 = 0.01$ (one of the values used in the analysis part) this requires $N \geq 10000$.

Chapter 6

Data processing

The main idea of the methods presented here is to find ways of exploiting the well developed tools from CMB physics to study heavy ion collisions.

For the data processing several tools have to be utilised. Before any programs can be used to do operations on the data it has to be in a suitable data format first. In section 6.1 the issue of the cylindrical nature of a heavy ion detector is addressed, as well as how it may be represented in a manner similar to CMB data for the analysis. The CMB program GLESP (Gauss-LEgendre Sky Pixelization)[49] is commonly used in CMB physics for calculations, manipulations etc. on CMB sky maps. In section 6.2 the utilisation of GLESP for the benefit of the analysis of heavy ion collisions is presented, and the pixelisation explained.

6.1 Conversion of a heavy ion signal

The heavy ion signal is cylindrical, as this is the shape of the detector. However, since CMB methods are developed for a spherical signal the heavy ion signal is converted to a spherical one. In figure 6.1 the coordinate shift is shown, were a spherical system of coordinates is imposed on the cylindrical one. The plane in the figure corresponds to $z = 0$. In spherical coordinates ϕ runs in the ***x*-*y*** plane, and θ from **+*z*** to **-*z***.

The transformation is very simply done by converting the (η, ϕ) coordinate of a particle (in radians) to (θ, ϕ) (in degrees), using $\eta = -\ln(\tan(\theta/2))$. Then the signal is decomposed into spherical harmonics as is customary in CMB analysis by using the package GLESP, which is also used for further analysis of the data.

6.2 GLESP

GLESP [49] is a program package developed for analysing CMB maps, such as those presented in figure 3.1. It can be used to do analysis on a map itself or decompose it into spherical harmonics and do calculations directly on a_{lm}'s. Furthermore one can do arithmetic operations on both maps and a_{lm}'s, apply masks, and much more[14]. The GLESP maps can be made using two

[14] See www.glesp.nbi.dk for a full description of the program.

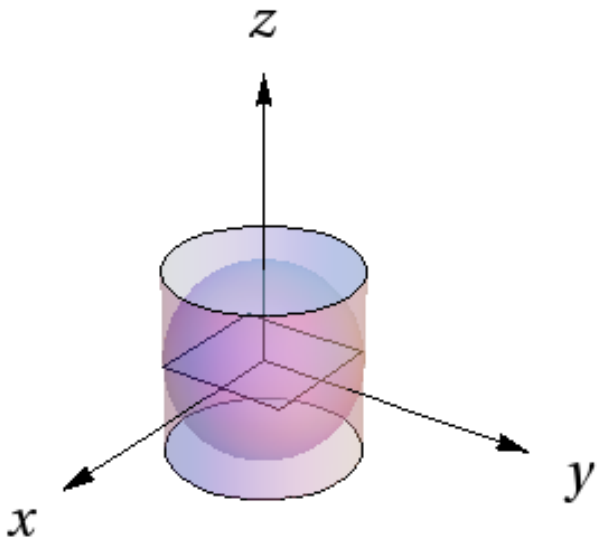

Figure 6.1: The set-up of coordinates. The cylinder represents the ALICE detector, which is then projected onto the sphere. The z-axis is pointed into the beam direction. The x axis points either into the center of the collider ring or away from the center, depending on the standard of the experiment in question. Figure by J. Kim.

kinds of pixelisation. For this thesis the "n" pixelisation was used (see section 6.2.1). Maps can be visually presented in a Mollweide projection. A Mollweide projection is a way of presenting a three-dimensional spherical signal in two dimensions, and is commonly used for maps of the Earth or the sky.

The output of the heavy ion simulations is a list of particles. Each line corresponds to one particle, and has information on its position (η, θ, ϕ) and possibly on the z-vertex (the exact point on the *z*-axis for the collision), input reaction plane angle (Ψ_R) and centrality. To convert this list to a GLESP map, the command $mappat$ is used. $mappat$ converts CMB maps from .ASCII format to .fits format, or converts a list of particles (.ASCII) to an heavy ion map (.fits)[15]. After making a map, the decomposition into spherical harmonics coefficients is done by the command $cl2map$. $cl2map$ can make maps based on a power spectrum or from a list of a_{lm}'s. It can also compute the power spectrum or a_{lm}'s from a map. $alm2dl$ does calculations on a_{lm}'s. It can also be used to convert an alm.fits file to .ASCII format. To visualize a map the command $f2fig$ can convert a .fits map to a .gif file.

Here $cl2map$ is used to find the spherical harmonics coefficients from the ALICE map, and $alm2dl$ is used to produce the corresponding power spectrum and a .ASCII file of the a_{lm}'s. The computation of $|a_{22}|/|a_{20}|$ is done in IDL.

In appendix B all used commands are listed and flags are explained.

[15]The implementation of processing an heavy ion map in GLESP was done by Oleg Verkhodanov, Special Astrophysical Observatory, Russian Academy of Sciences, Nizniy Arkhiz, Russia

6.2.1 Pixelisation

The pixelisation used for the data analysis is the "n" pixelisation in GLESP [50]. It is illustrated in figure 6.2. Each latitude has the same number of pixels. Thus, the poles and the equator has the same number of pixels, but different pixel size.

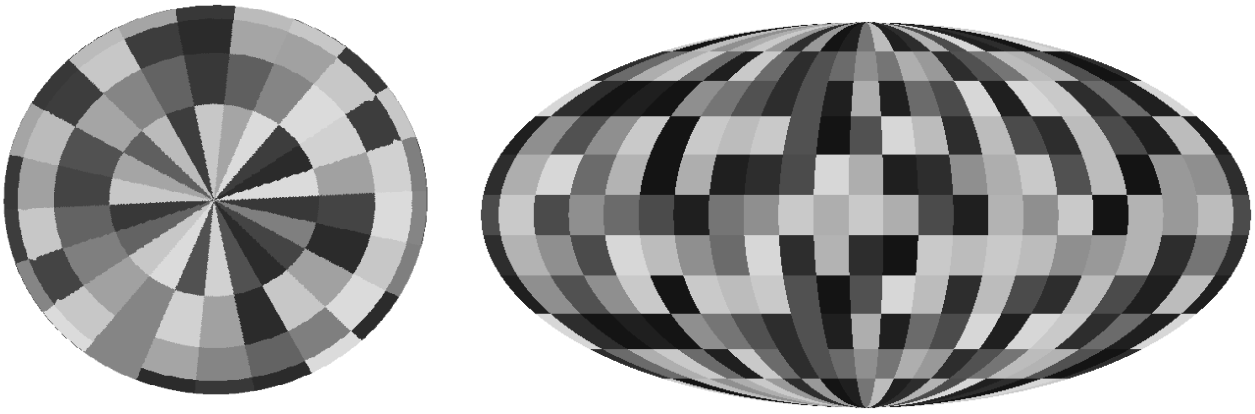

Figure 6.2: GLESP "n" pixelisation. To the left the polar cap is shown, and to the right a Mollweide projection of a map in n pixelisation is shown. Figure from [50]

Part III

Data analysis

Chapter 7

Analysis of toy model simulations of heavy ion collisions

The analysis part of this thesis is split into two chapters. Firstly, a toy model is tested to establish whether the tools and methods presented in chapter 5 & 6 are viable at all for determining the amplitude of flow and give sensible results that can be of use in heavy ion physics. It is important to ensure this by firstly using a toy model because of the computational time required for more complex simulations. Secondly, a more sophisticated model is used, to see if the methods are also applicable on relatively complex simulations. This chapter will cover the analysis of the toy model, and chapter 8 will cover the analysis of simulations using HIJING (Heavy-Ion Jet INteraction Generator) - an event generator commonly used in heavy ion physics.

The aim of the analysis is to ultimately determine the amplitude of elliptic flow on an event-by-event basis, and secondly to investigate the reaction plane angle (only for the HIJING simulations).

The work presented in this thesis has been done in collaboration with the heavy ion group at the Discovery Center, which has been responsible for the production of simulated data. The processing and analysis of this provided data is the subject of this thesis. Therefore, a detailed description of the models used to simulate data will not be presented here.

Since this is a very preliminary study of the application of new methods on collisions, not all features that are expected in real events are included. It is important to control as many parameters and dependencies as possible and show how the methods perform under these conditions before a full analysis of complex simulations is done. Thus, v_2 is constant with θ and no dependence on transverse momentum or particle identity (e.g. baryons and mesons) is included. Also, no higher order flow is induced.

7.1 Model and simulation

The toy model simulates an event as a Gaussian distribution in η (pseudorapidity) generated by a Monte Carlo generator (using a random number generator). This of course also gives statistical fluctuations. The Monte Carlo generator and model was partly written by Jens Jørgen

Gaardhøje, NBI, and partly uses the ROOT analysis package [51]. In figure 7.1 the pseudo-rapidity density and the corresponding density in θ is plotted, to show how the particles are distributed. The multiplicity is set to 30000 particles.

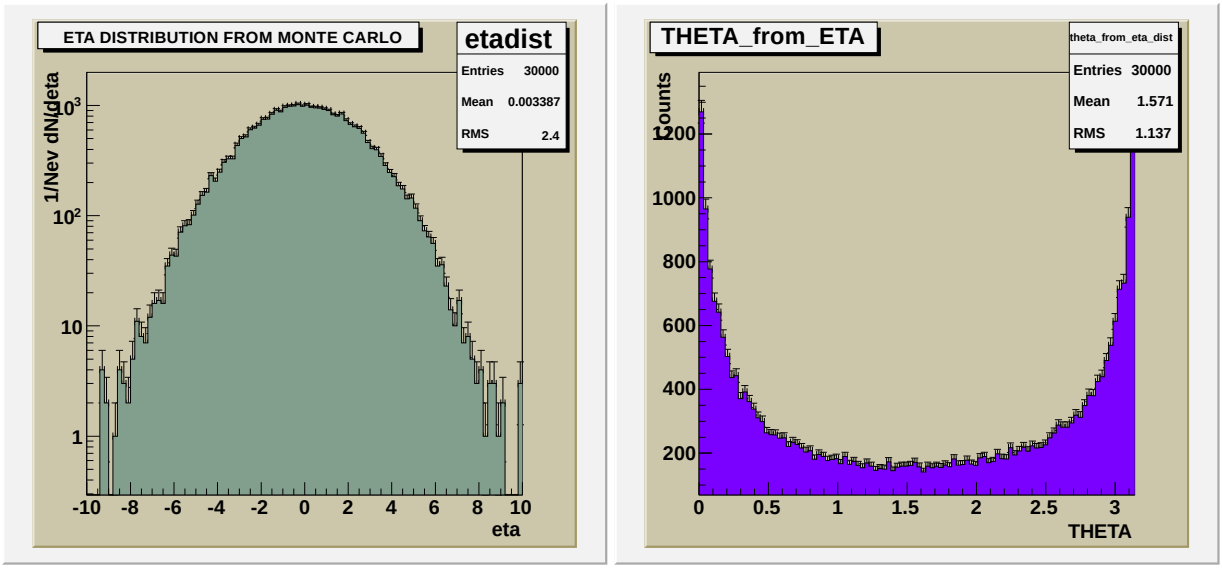

Figure 7.1: Left: $dN/d\eta$, the pseudorapidity density as a function of η. It follows a Gaussian distribution with statistical fluctuations. Right: The corresponding $dN/d\theta$ distribution, by using Eq.(4.1). Figure produced by J. J. Gaardhøje

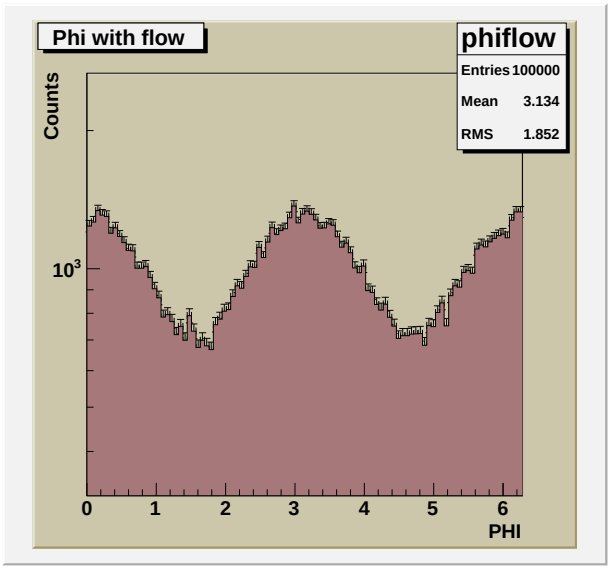

Figure 7.2: Flow induced in the signal by modulating in the ϕ direction, according to Eq.(4.3). Figure produced by J. J. Gaardhøje

These basic simulated events may afterwards be induced with additional effects, such as flow or jets. Here the focus is on elliptic flow, $n = 2$. To keep the simplest configuration

possible, Ψ_R is set to zero. Since it only induces a shift in ϕ of the modulation but does not alter the amplitude this can be done without loss of flow information. In figure 7.2 the modulated equivalent of figure 7.1 is shown. Note that here the multiplicity is 100,000. The cosine nature of the flow modulation is easily seen.

The output of the program is a list of particle coordinates. Only the spatial distribution of particles is of interest in this model, in order to study the morphology of the event. The simulated data was processed using GLESP, as described in section 6.2. The list of spatial coordinates for each particle was converted to a map of the event and a file of corresponding a_{lm}'s was produced. The power spectrum was also calculated using GLESP.

7.2 Background

What is defined as a background in the simulations, is the kinematic background of a collision with no effects (such as flow, jets, etc.). There will be a larger amount of particles in the beam directions than orthogonal to the beam, as described in section 5.3.1. In figure 7.3(left), this kinematic background is presented from a simulation with $v_2 = 0$ and multiplicity of 30000. The resolution corresponds to $l_{max} = 100$. The poles (top and bottom) correspond to the beam directions, whereas the equator is 90^o to the beam.

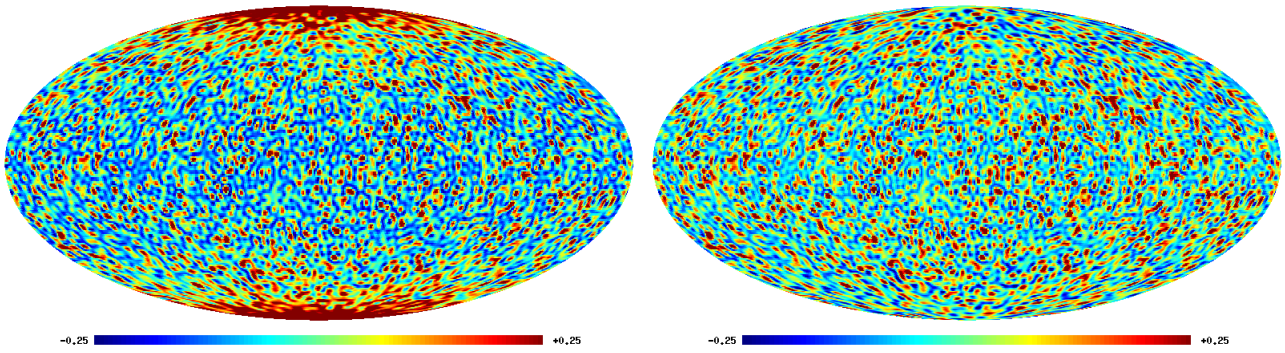

Figure 7.3: Left: one simulation of the total kinematic background, all modes included. Right: The same simulation with the $m = 0$ mode removed.

In figure 7.4, the power spectrum of one kinematic background realisation is plotted. In accordance with the argumentation in section 5.3.1 the $m = 0$ mode is removed in order to see the finer features of the background (the effect is also easily seen in figure 7.3).

The map and power spectrum of a background without modulation serve as reference to the simulations where the signal has been modulated.

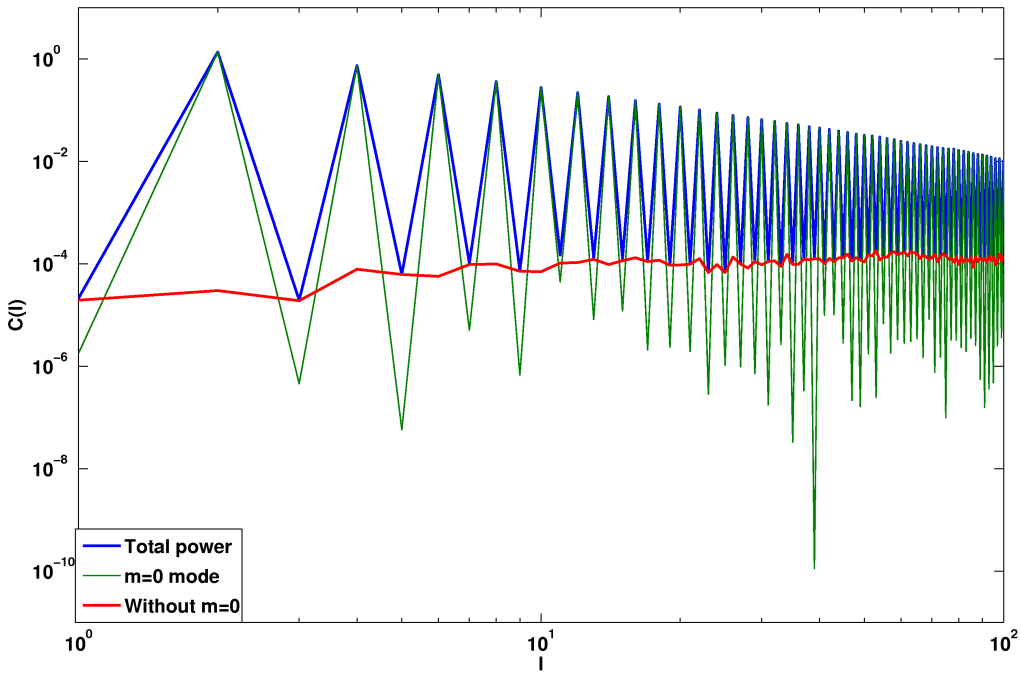

Figure 7.4: Power spectrum for the kinematic background. The blue curve is the total power spectrum (all m modes), the green is only for the m=0 mode, and the red is for $m \geq 1$.

7.3 Modulations of the signal

In this section, flow of varying strength is induced in the ϕ direction. The modulation is shown in figures 7.5 (v_2 = 0.05) and 7.6 (v_2 = 0.3). The strong flow, v_2 = 0.3, is included to show very visually the effects of such a modulation, while the v_2 = 0.05 is a realistic value for the flow in an actual collision. $v_2 = 0.05$ is not visible from the map itself, whereas $v_2 = 0.3$ is very clearly seen.

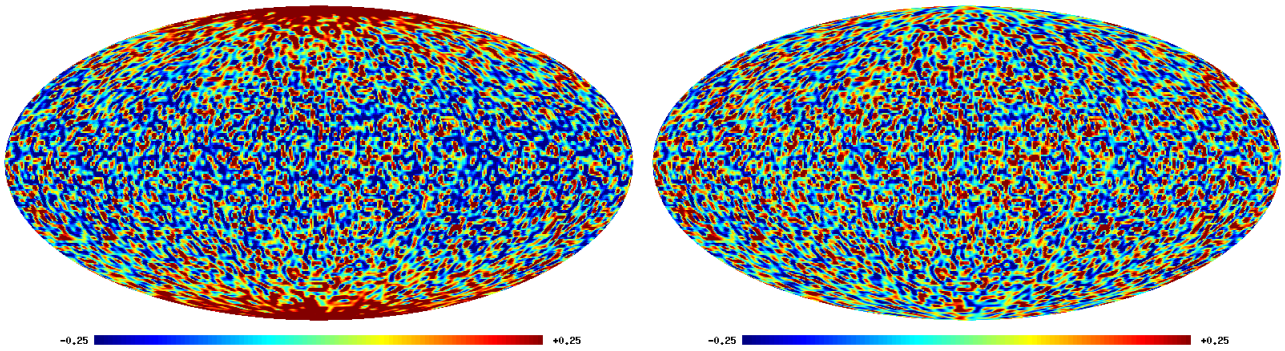

Figure 7.5: Maps for a simulation with a modulation by flow in the ϕ direction, with a realistic value for the flow: v_2 = 0.05. Left: Total map. Right: $m = 0$ mode removed.

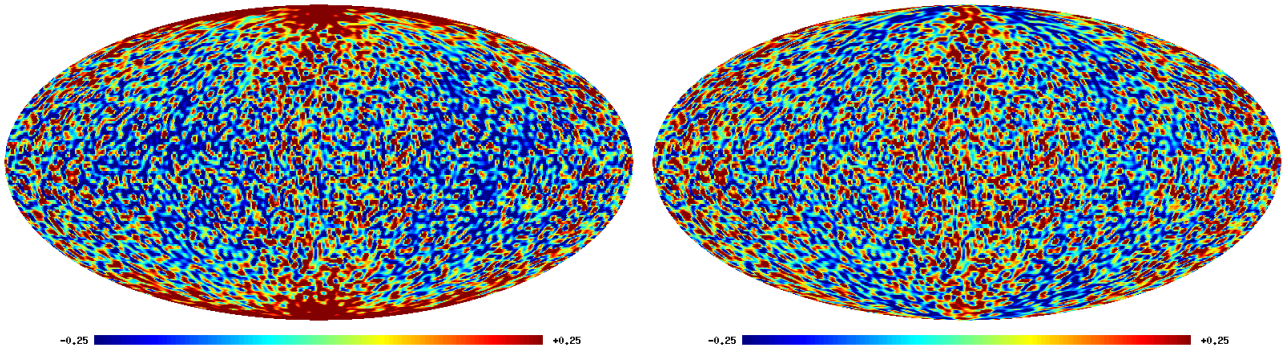

Figure 7.6: Maps for a simulation with a modulation by flow in the ϕ direction, with a high value for the flow: v_2 = 0.3. Left: Total map. Right: $m = 0$ mode removed.

The power spectrum for four amplitudes of flow is depicted in figure 7.7. The total power spectrum for the four different flow amplitudes is more or less the same, but the power spectra for $m \geq 1$ are very different. This is to be expected, because the background (section 5.3.1) dominates over the effect of flow in the total power spectrum. Because elliptic flow contributes mostly into the even multipoles, especially at low l, a higher amplitude of flow causes higher power at these multipoles. This is clearly seen in the power spectra.

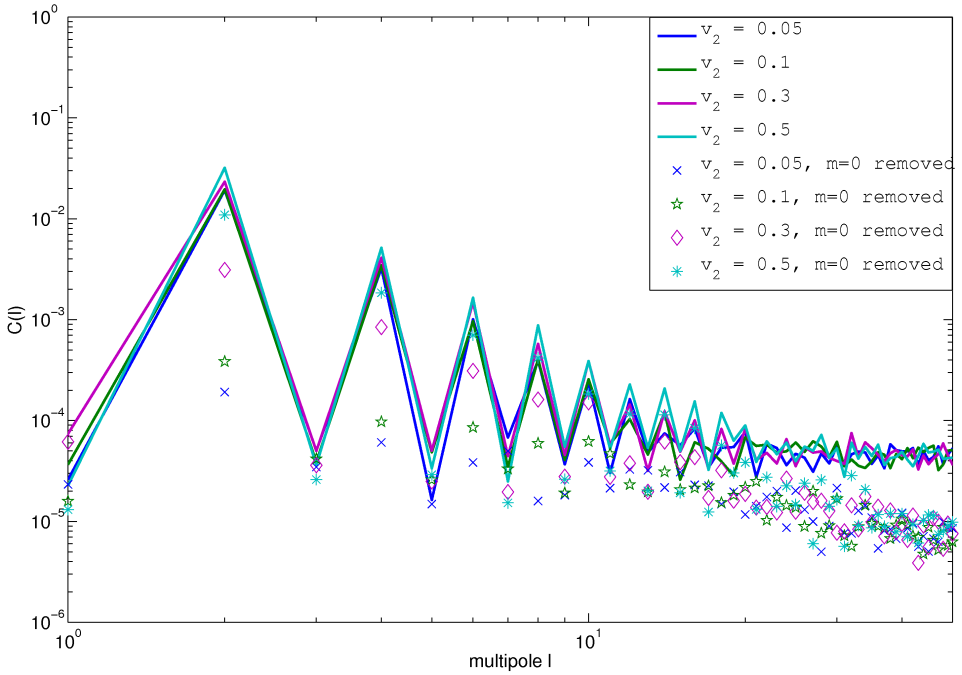

Figure 7.7: Power spectrum for four amplitudes of flow. The lines represents the full power spectra, the dots the power spectra with the $m = 0$ mode removed. Note that the axes have logarithmic scale.

As argued in section 5.3.2, elliptic flow is the only flow moment contributing to the a_{22} component. Thus, mapping a_{22} for different amplitudes of elliptic flow is a clear visual indication of the contribution of elliptic flow into a_{22}. One expects the component to become more pow-

erful with increasing flow. This is indeed the case in figure 7.8. The signature of a_{22} for $v_2 = 0$ is fundamentally different from the ones with flow, and the higher the flow the more powerful a_{22} becomes. As mentioned in section 7.1, $\Psi_R = 0$. A different reaction plane angle would manifest itself as a phase shift in the 'East-West' direction.

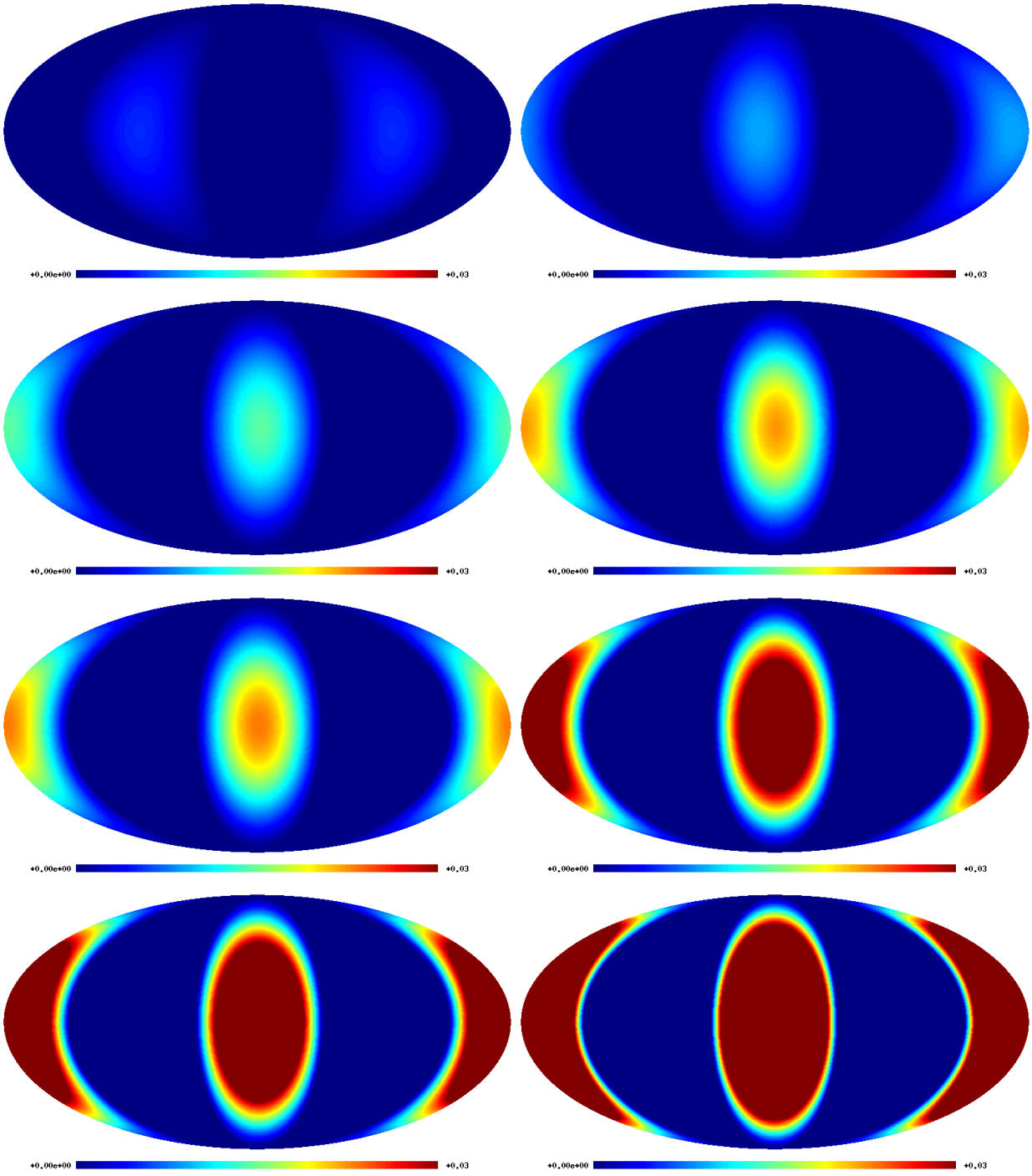

Figure 7.8: From the top left down to the bottom right: Maps of a_{22} for representative input flow values of $v_2 = 0, 0.01, 0.05, 0.075, 0.1, 0.2, 0.3, 0.5$, respectively. For simplicity $\Psi_R = 0$ in all maps.

7.3.1 $a_{2,2}$ analysis

To obtain the amplitude of elliptic flow in an event the a_{22} analysis method is used, as presented in section 5.3.2. The idea is to take advantage of the fact that only v_2 is contributing to the $l = 2$, $m = 2$ component of the spherical harmonics coefficients of a given map. One takes the ratio

$$\frac{|a_{22}|}{|a_{20}|} \approx v_2. \tag{7.1}$$

The dataset contains one event per amplitude of flow. The ratio was calculated for each event and plotted against the input v_2, see figure 7.9. The plot clearly shows that the theory holds, as the regression gives a fit of $\frac{|a_{22}|}{|a_{20}|} = v_2 * 1.09 + 0.00888$. Thus, this method seems viable for determining the amplitude of elliptic flow on an event-by-event basis. The error bars are estimated by $\frac{|a_{21}|}{|a_{20}|}$, as described in section 5.3.3. Note that the regression is made for the values of $\frac{|a_{22}|}{|a_{20}|}$ only, and does not take the error bars into account.

The slight deviation from perfect 1:1 correlation is probably an experimental calibration factor. It can be due to the fact that when the amplitude of flow becomes too low, $\frac{|a_{22}|}{|a_{20}|}$ is dominated by random noise and cannot determine v_2. This is expected at $v_2 \lesssim 0.01$. Thus the data points at $v_2 = 0.01$ and $v_2 = 0$ are 'contaminating' factors in the fit. Another explanation is the limited resolution for the decomposition into a_{lm}'s by $l_{max} = 100$, since the theoretical formula in principle assumes infinitely good resolution. Furthermore the theoretical formula is based on the assumption that $|c_{2,2}| \ll v_2|c_{2,0}|$ (or equivalently $\frac{|c_{2,2}|}{v_2|c_{2,0}|} \ll 1$). The validity of this assumption is tested in table 7.1. Note that $c_{2,0}$ is for the background without any flow modulation, whereas $a_{2,0}$ would be the total signal with flow modulation. Thus $|c_{2,2}|$ and $|c_{2,0}|$ are the same for all values of v_2.

v_2	$\lvert c_{2,2}\rvert / v_2 \lvert c_{2,0}\rvert$
0.01	0.7233
0.05	0.1447
0.075	0.09644
0.1	0.07233
0.2	0.03617
0.3	0.02411
0.5	0.01447

Table 7.1: Test of $\frac{|c_{2,2}|}{v_2|c_{2,0}|} \ll 1$ assumption for toy model.

Except for $v_2 = 0.01$, and to some degree also $v_2 = 0.05$ the assumption seems legit.

In conclusion, the methods from chapter 5 perform very well in the analysis of the toy model. The elliptic flow amplitude of an event is reconstructible with very good agreement with the input flow, and shows a tight linear trend for increasing flow amplitudes as predicted by the model.

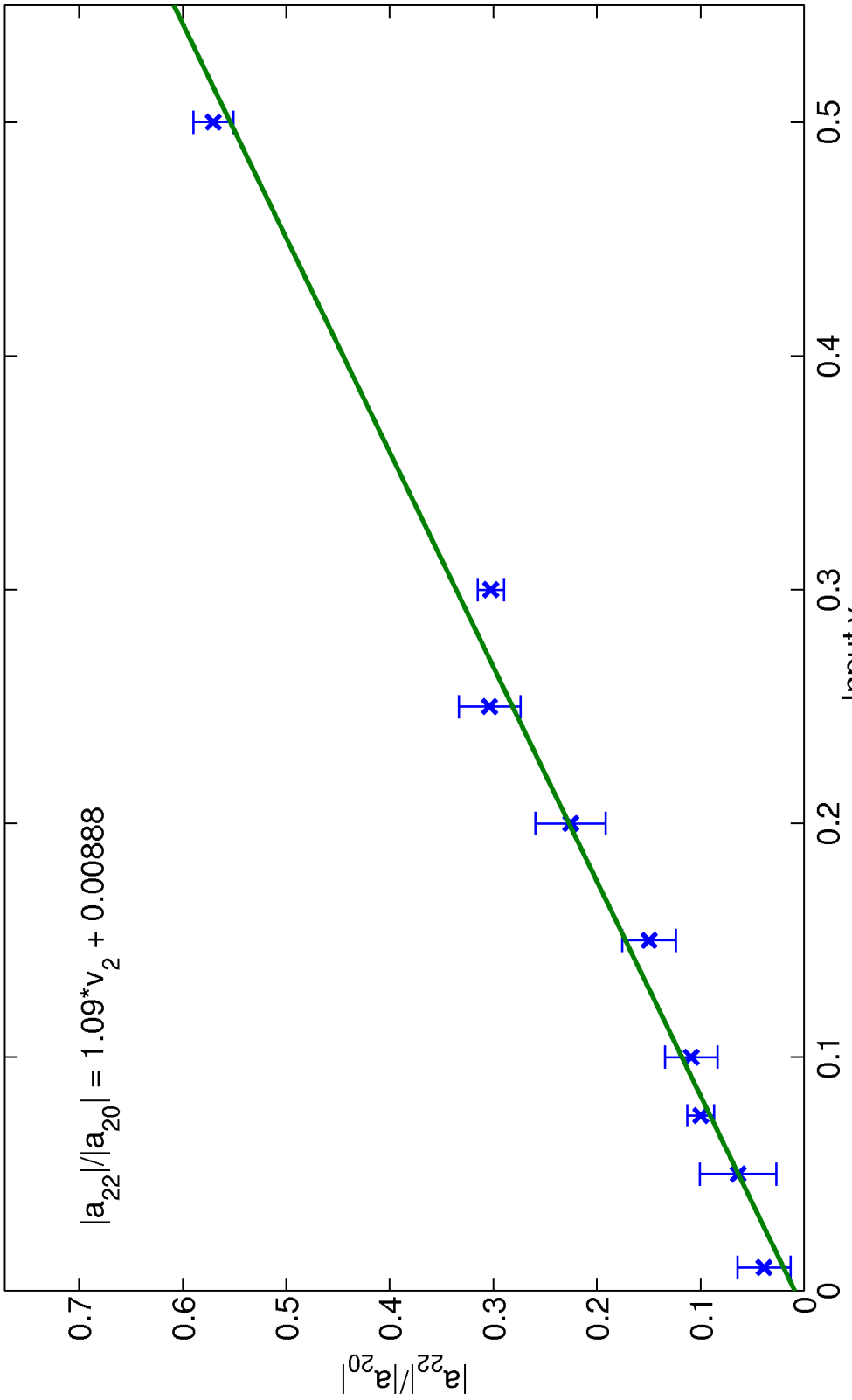

Figure 7.9: $\frac{|a_{22}|}{|a_{20}|}$ *as a function of the input* v_2.

Chapter 8

Analysis of HIJING simulations

Since the analysis of toy model simulations proved to be quite promising (as presented in the previous chapter), further analysis is undertaken with a more complex model for simulations. Whereas the toy model was simply based on a random generator, this chapter will use the HIJING [52] event generator developed (and commonly used) by the heavy ion community for more sophisticated simulations of heavy ion collisions[16].

The objective of this chapter is to see if results similar to those in figure 7.9 can be obtained, as well as a determination of the event plane angle, Ψ_n, for different amplitudes of flow. Whereas the toy model focused on a broad range of flow amplitudes, this chapter will limit itself to physically realistic flow amplitudes.

The analysis presented here only uses pure Monte Carlo simulations and does not take detector effects into consideration. Simulations with detector effects take into account the fact that a detector never has full acceptance over the full ϕ or θ range. This causes 'holes' in the total map of the event, where particles are either not detected at all or are only detected with some reduced acceptance. Since this is indeed the case for real collision data it would be interesting to apply the methods to such simulations, but this is beyond the scope of this thesis and will have to be covered in future work instead. Thus, all produced particles are assumed observed with uniform acceptance but still with a resolution limited by $l_{max} = 100$.

8.1 Model and simulation

HIJING uses physics to simulate the outcoming particles and their distribution. The initial geometry, impact parameter, number of participating nucleons and the distribution of the matter is determined by a Glauber model [30] event-by-event. HIJING reproduces some of the main features of heavy ion collisions at the RHIC and LHC energies. It does not, however, include collective flow. Instead flow is induced a posteriori using an "afterburner"[17]. Just as for the toy model no η, particle species or p_t dependence of the flow is included in the model, in order to keep the setup as simple as possible. Also, no higher order flow is induced. However, each

[16] The simulation of data has been undertaken by the heavy ion group as part of the collaboration, and the author has therefore not been directly involved in their production.

[17] The AliGenAfterBurnerFlow developed by the ALICE experiment at CERN.

event is supplied with a randomly chosen reaction plane angle, Ψ_R, which is set to be Ψ_2. This only shifts the signal in the ϕ direction, and has no influence on the amplitude of the flow. Ψ_n is included in the HIJING simulations because the method derived in chapter 5 also includes a way of determining Ψ_n, which is worth investigating.

HIJING produces events with distributions in (η, ϕ) or (θ, ϕ) quite similar to the toy model. Figures corresponding to figure 7.1 are presented in figure 8.1. Figure 8.2 corresponds to figure 7.2. Note that figure 7.2 is made for an event with a multiplicity of 100,000, whereas figure 8.2 is for an event with a multiplicity of 10,802.

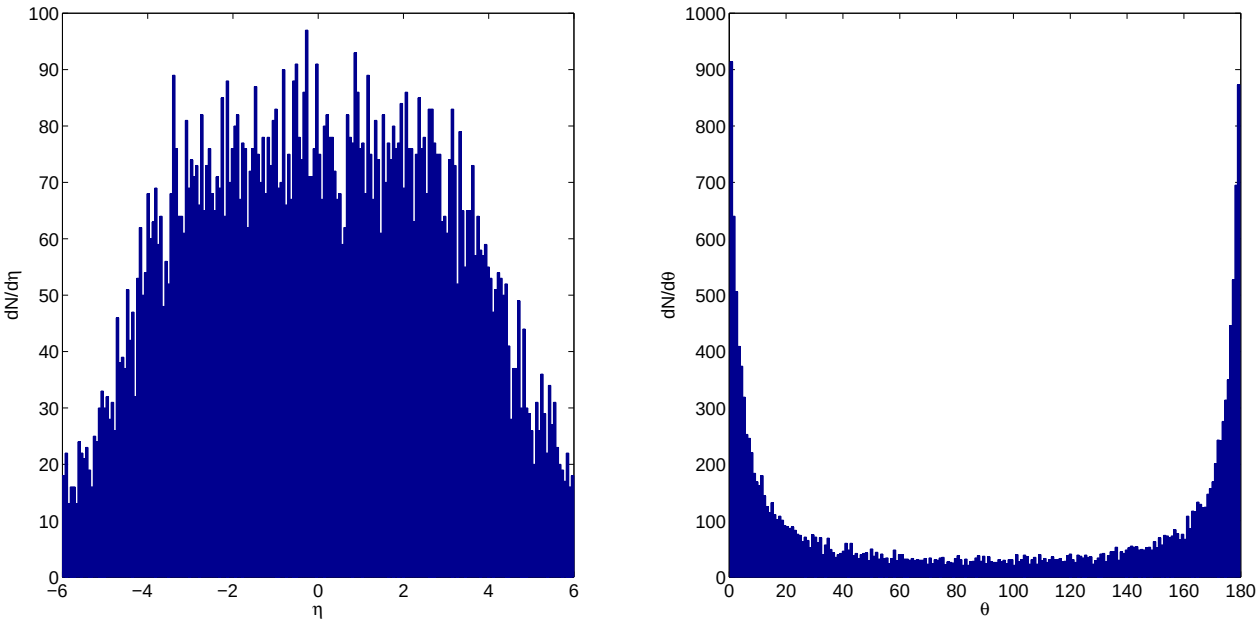

Figure 8.1: Left: Pseudorapidity density of particles for one HIJING simulation ($v_2 = 0$). Right: same plot, in polar coordinates. Number of bins is 200, multiplicity is 17,782.

The fluctuations in the simulation are quite large, which might be problematic for the a_{22} analysis because it assumes that the statistical noise is much smaller than the total signal (for a Gaussian distribution at a multiplicity of 10,802 the statistical noise should be comparable to $\sim 1\%$). The fit in figure 8.2 is done using Eq.(5.5), and has a goodness of fit[18]of $R^2 = 0.7285$, which reflects the influence of the large fluctuations.

[18] R^2 measures how successful the fit is in explaining the variation of the data. R^2=1 is a perfect fit. A R^2 value of 0.7285 means that the fit explains 72.85% of the total variation in the data about the average.

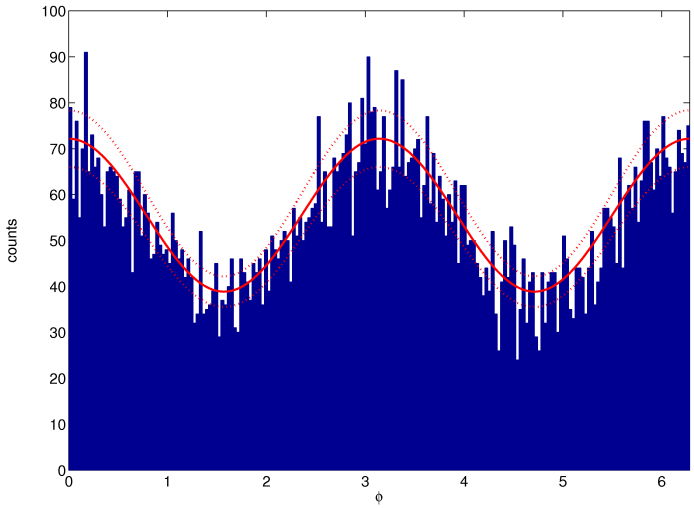

Figure 8.2: Density of particles as a function of azimuthal angle, ϕ. Simulation using HIJING and modulated by an elliptic flow of $v_2 = 0.15$. The red line is a fit with fixed v_2=0.15 to the distribution. The dotted lines show the 95% confidence level of the fit. Number of bins is 200.

8.2 Flow

The difference in statistical properties for the HIJING simulations and toy model simulations might affect the applicability of the a_{22} method derived in chapter 5. This is investigated in section 8.2.1. To visualise the flow, a map of a HIJING simulation with flow ($v_2 = 0.15$) is shown in figure 8.3.

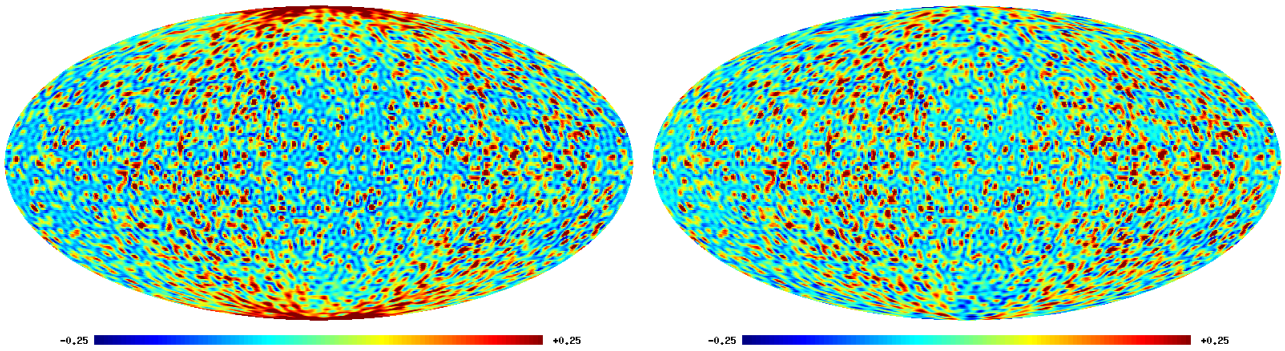

Figure 8.3: Maps of a HIJING simulation with $v_2 = 0.15$ and multiplicity 10802 ($1 \leq l \leq 100$). Left: all modes included. Right: $m = 0$ mode removed. $\Psi_2 = 1.23$ (rad.)

Mapping a_{22} is a clear way of visually presenting the effect flow has on the coefficient. The amplitude of a_{22} is expected to grow with increasing flow amplitude, as can also be seen from figure 8.4. Note that each map has been rotated by $\phi - \Psi_R$, to be easily comparable.

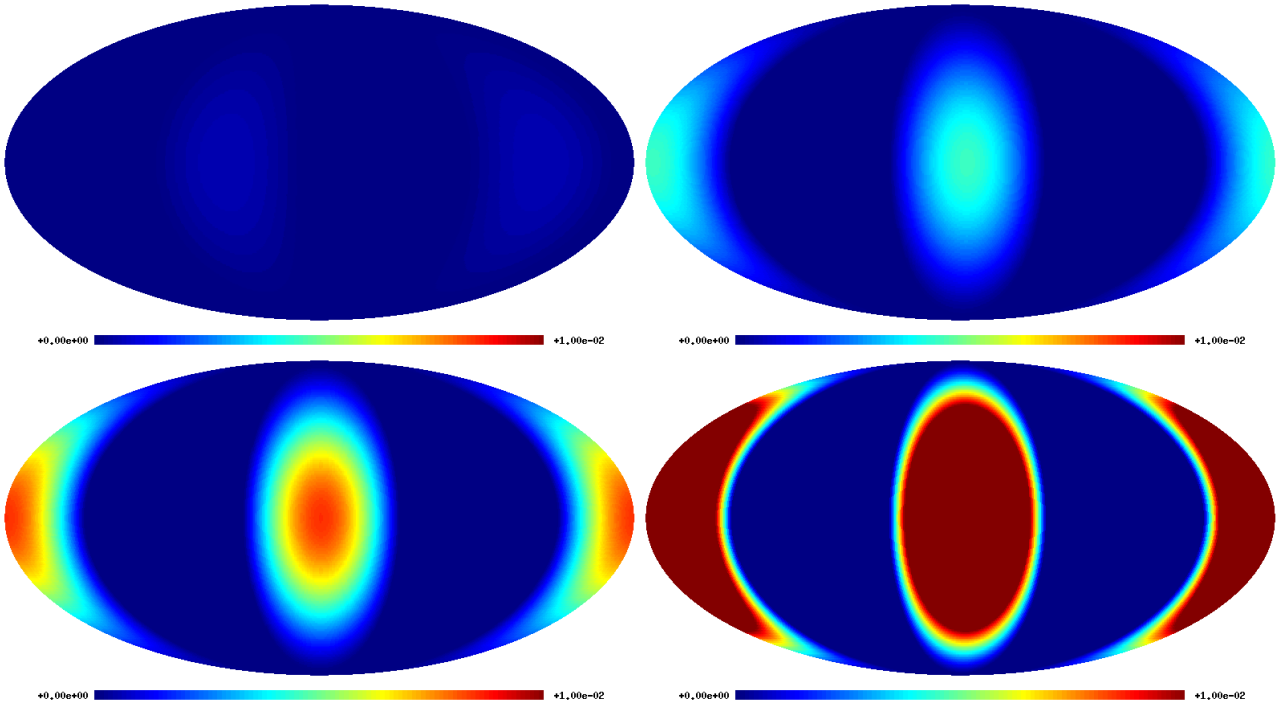

Figure 8.4: From the top left down to the bottom right: Maps of the $|a_{22}|$ amplitude for input flow values of $v_2 = 0, 0.01, 0.05, 0.07$, respectively. The maps have been rotated by the input Ψ_R.

8.2.1 $a_{2,2}$ analysis

The main task is to extract information about the amplitude of the input elliptic flow and the reaction plane angle (in practice the event plane angle). Contrary to the toy model investigation an ensemble of events was produced for 5 values of flow, and a reference with $v_2 = 0$. In total 630 event for each flow amplitude was produced. However, a HIJING simulation is based on random generation of how the two nuclei collide, and thus also the multiplicity of the event. Thus a selection on the multiplicity has to be used, to avoid dominance of statistical noise (see section 5.3.4). The selection is presented in table 8.1. The multiplicity of the 630 events per flow range from of $\sim$ 10 to $\sim$ 30000. The selection is chosen to be high enough for $v_2 = 0.01$ to just exceed the level of statistical noise (for events of $\sim$ 10000 it is just at the level of statistical noise). A higher cut on the multiplicity would lower statistical noise, but would result in a very small ensemble of events.

v_2	Selection	# events
0.00	$10000 \leq N_{mult} < 30000$	71
0.01	$10000 \leq N_{mult} < 30000$	135
0.0375	$10000 \leq N_{mult} < 30000$	105
0.05	$10000 \leq N_{mult} < 30000$	124
0.07	$10000 \leq N_{mult} < 30000$	164
0.15	$10000 \leq N_{mult} < 30000$	114

Table 8.1: Selection for the events. N_{mult} is the multiplicity.

The distributions in figures 8.1 and 8.2 suggested that the level of noise is larger for the HIJING simulations than for the toy model. Before the data analysis is undertaken, a test of the assumptions in section 5.3.2 is therefore in place. A key assumption is that the $m = 0$ mode is the most dominating component of the signal, and thus that $v_2|c_{2,0}| \gg |c_{2,2}|$ (or equivalently $\frac{|c_{2,2}|}{v_2|c_{2,0}|} \ll 1$). This is tested in table 8.2. Here $|c_{2,2}|$ and $|c_{2,0}|$ are averages of the 71 events with $v_2 = 0$. The table should be compared to table 7.1.

v_2	$\frac{\lvert c_{2,2}\rvert}{v_2\lvert c_{2,0}\rvert}$
0.01	2.160
0.0375	0.5760
0.05	0.4320
0.07	0.3086
0.15	0.1440

Table 8.2: Test of $\frac{|c_{2,2}|}{v_2|c_{2,0}|} \ll 1$ assumption for HIJING events.

For $v_2 = 0.01$ the approximation is not valid, which is expectable since $v_2 = 0.01$ is at the level of the statistical noise. For $v_2 = 0.0375, 0.5$ and 0.7 the fraction $\frac{|c_{2,2}|}{v_2|c_{2,0}|}$ is non-negligible, and only for $v_2 = 0.15$ does it begin to approach order 10%. This indicates that the derived

$$\frac{|a_{22}|}{|a_{20}|} \approx v_2. \tag{8.1}$$

relationship will have some correction factor. Just as for the toy model, the limited resolution due to the choice of $l_{max} = 100$ will also cause a deviation from a pure 1:1 correlation.

Furthermore, in figure 8.3 it seems as if there is a tilt of the symmetry plane of the flow - it does not coincide with the θ direction. A tilt would induce a θ-dependence of the data, mimicking a θ dependent v_2. Such a tilt would show up in e.g. the $|a_{21}|$ component in respect to the $|a_{22}|$ component, since a_{21} represents both θ and ϕ dependence (see figure 3.5, middle). In table 8.3 this is shown to be the case for the HIJING simulations; $|a_{21}|$ is between 20-100% of the $|a_{22}|$ component for $v_2 = 0.01 - 0.05$. Comparing to the toy model, where the fraction is $\frac{|a_{2,1}|}{|a_{2,2}|} = 0.13$ for $v_2 = 0.075$ for just one event, whereas for the HIJING simulations the *average* over 124 events for $v_2 = 0.07$ is 0.1948 with a spread of ~ 0.10.

v_2	$\frac{\langle\lvert a_{2,1}\rvert\rangle}{\langle\lvert a_{2,2}\rvert\rangle}$
0.00	1.445
0.01	1.462
0.0375	0.4872
0.05	0.3001
0.07	0.1948
0.15	0.09815

Table 8.3: Test of $\frac{|c_{2,2}|}{v_2|c_{2,0}|} \ll 1$ assumption for HIJING events.

Even so, the data is plotted in figure 8.5, which is the HIJING equivalent to figure 7.9. The error bars are 1σ deviations calculated from the ensemble for each flow value.

The regression is only with respect to the points (crosses) that represent the mean of $|a_{22}|/|a_{20}|$ of the ensemble for each input flow amplitude. It does not take the error bars into consideration, just as the data points for $v_2 = 0.01$ and $v_2 = 0$ are not used, because they are on the level of the statistical noise. Another regression with higher or lower inclination is also possible within the error bars. The regression is still useful because it clearly shows the linear relationship.

The original equation, Eq.(5.16), does not take a θ dependence of the signal into account, and thus cannot predict the behaviour in figure 8.5 perfectly. The factor of 1.81 (~ 2) is related to both the breakdown of the assumptions on the dominance of $v_2|c_{20}|$ and the tilt of the signal. As was also the case for the toy model, the limited resolution also contributes into this calibration factor.

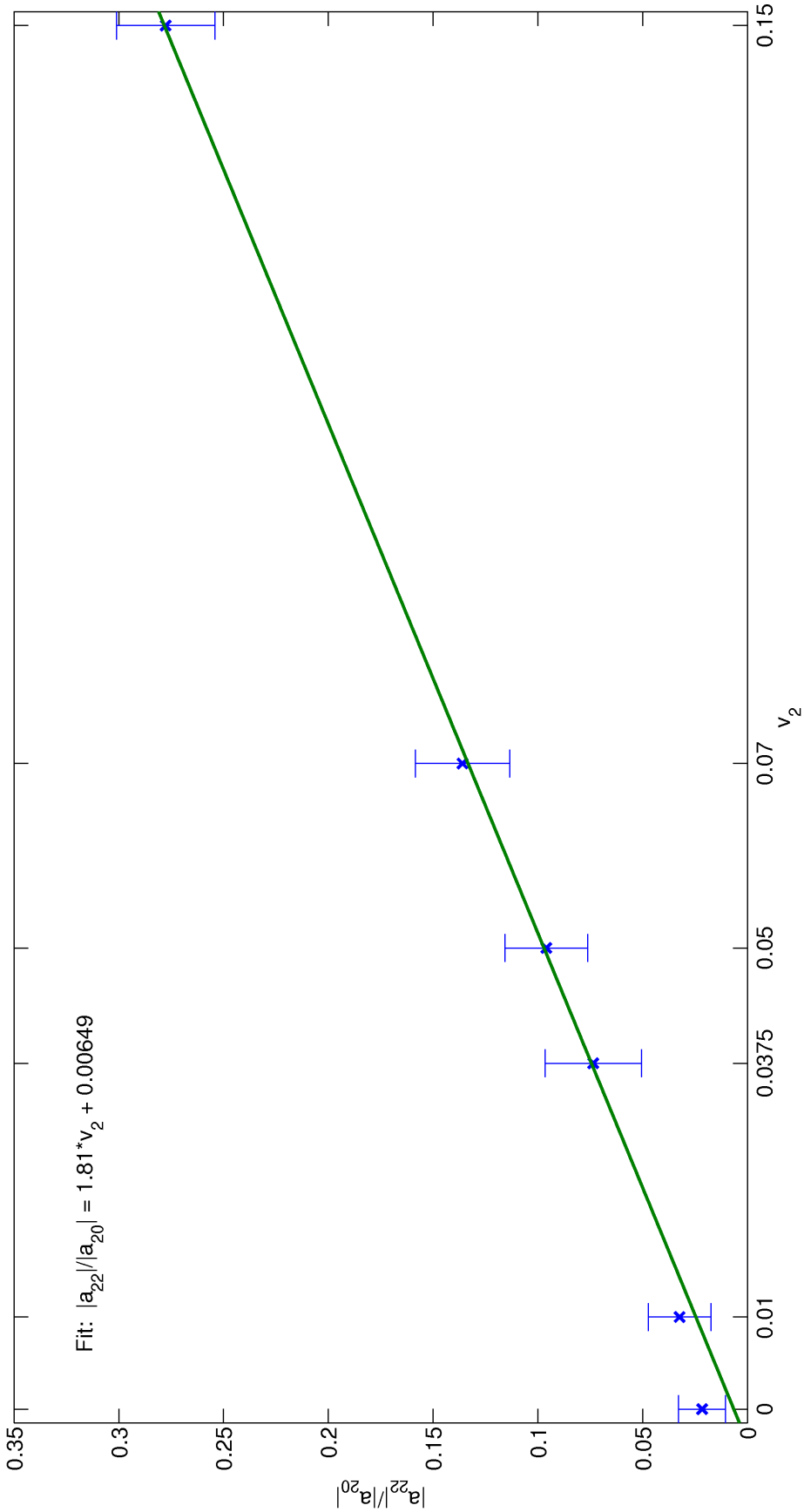

Figure 8.5: $\frac{|a_{22}|}{|a_{20}|}$ as a function of the input v_2. Error bars are 1σ.

8.2.2 Error estimation for HIJING simulations

The aim of the analysis presented in sections 7.3.1 and 8.2.1 has been to be able to determine the amplitude of elliptic flow on an event-by-event basis. In the analysis of HIJING data 630 events (after selection on high-multiplicity only ~ 100 events) for each amplitude have been analysed, which makes statistical error analysis over an ensemble of events possible. This includes a measure for the uncertainty and error by taking the standard deviation of the sample. Taking the standard deviation of a data sample to be the 68% confidence level requires Gaussianity of the data. The validity of this assumption is shown in figure 8.6.

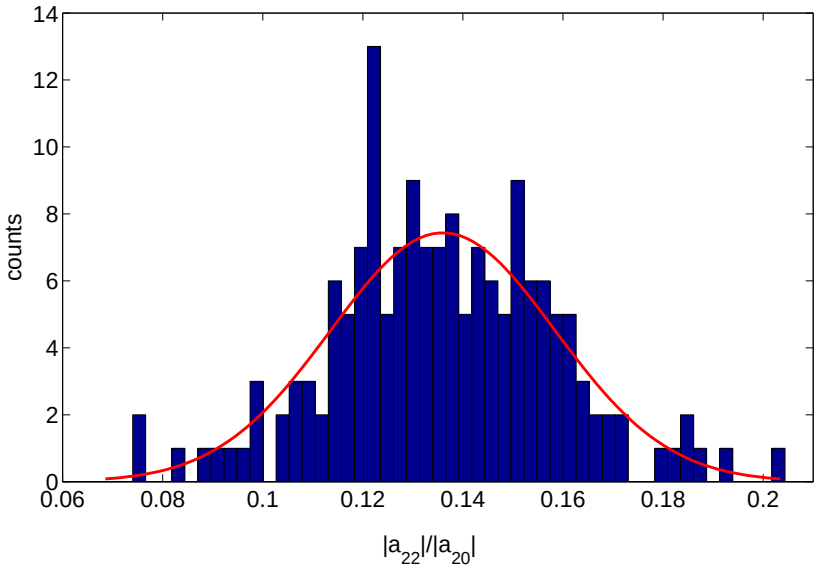

Figure 8.6: Gaussianity of data for $v_2 = 0.07$. Number of bins = 50.

The use of standard deviations is not viable for a single event. It is still necessary, though, to provide a measure of how exact the results are, and what the errors on the output flow amplitude should be. In section 5.3.3 it was postulated that $\frac{|a_{21}|}{|a_{20}|}$ is a good measure for the uncertainty of v_2 for an event, because there is no contribution from $n > 1$ flow into this fraction and because the statistical properties are the same as for $\frac{|a_{22}|}{|a_{20}|}$.

In table 8.4 this postulate is tested and the errors on the a_{22} results are presented. $\frac{|a_{21}|}{|a_{20}|}$ is only a measure of the magnitude of statistical fluctuations.

v_2	$\langle \frac{\lvert a_{22}\rvert}{\lvert a_{20}\rvert} \rangle$	σ	$\langle \sigma_{21} \rangle$
0.00	0.0216	0.0112	0.0230
0.01	0.0324	0.0150	0.0295
0.0375	0.0736	0.0230	0.0304
0.05	0.0960	0.0197	0.0279
0.07	0.136	0.0225	0.0259
0.15	0.278	0.0235	0.0269

Table 8.4: Error estimation for high multiplicity events, $10000 \leq N_{part} < 30000$. $\sigma_{21} = \frac{|a_{21}|}{|a_{20}|}$

The first column is the value of the input flow. The second column is the mean of $\frac{|a_{22}|}{|a_{20}|}$ for the number of events as specified in table 8.1. The third column is the standard deviation of $\frac{|a_{22}|}{|a_{20}|}$ for the specified number of events. The fourth column is the mean of $\frac{|a_{21}|}{|a_{20}|}$.

$\frac{|a_{21}|}{|a_{20}|}$ is of the same order of magnitude as σ, but for $v_2 < 0.05$ it seems to overestimate the uncertainty. It was argued in the previous section that a tilt in the data would enhance the a_{21} component, in which case it is no longer a proper measure of the uncertainty. In order to use $\frac{|a_{21}|}{|a_{20}|}$ as the order of magnitude for the uncertainty, ones needs to correct for the tilt.

It is seen from the table that even though $v_2 = 0.0375$ should be above the level of statistical noise, the uncertainties are almost of the same amplitude as the signal itself, indicating that this is not the case. According to table 8.4 one should be careful with the determination of flow amplitude for $v_2 \lesssim 0.05$.

In conclusion, the results on the determination of the flow amplitude are not as promising for the HIJING simulations as they were for the toy model simulations. The level of noise and uncertainty is comparable to that of the values of flow for $v_2 \lesssim 0.07$. The linear correlation of $\frac{|a_{22}|}{|a_{20}|}$ and v_2 is confirmed though, indicating that the strategy of implementing CMB methods into the field of heavy ion collisions is still promising but needs more work. One possible direction for future work could be the investigation of either decreasing the significance of the noise or enhancing the signal of interest (e.g. using masks or window functions).

8.3 Determining Ψ_n

In addition to determining the flow amplitude, one is also interested in the reaction plane angle, Ψ_R (in practice Ψ_2). This was not found for the toy model since Ψ_R was set to zero. From the data Φ_{22} can be found for each event. Using the formula in Eq.(5.16), one can obtain the input Ψ_R. This is plotted in figure 8.7.

Figure 8.7 uses $v = 0.07$ with the selection presented in table 8.1. A linear relationship is clearly seen, with small deviations (order of ± 0.2 rad), which is in very good agreement with the theoretical formula, $2\Psi_n = \Phi_{22}$.

A note on the data analysis for Ψ_n: the definition of the ϕ-coordinate and the position of $\phi = 0$ is not the same for the simulation and the angle calculated from Eq.(3.2). The difference is the direction of the z axis, or equivalently θ, as well as a shift of the direction of $\phi = 0$ (orientation of the x-axis). Therefore a coordinate shift was done on ${\Psi_n}$[19]. The shift has nothing to do with Eq.(5.16), it is only a definition of the orientation of the coordinate system that is different in GLESP and the HIJING simulation.

In most cases, it is not proper scientific conduct to remove data points that seem wrong from a dataset. However, in the case of a cyclic signal the point s is the same as $s + p$, where p is the period. This is the case in figure 8.7. The two points at $(\Psi_R = \pi, \Phi_{22} \approx 0)$ and $(\Psi_R = 0, \Phi_{22} \approx 2\pi)$ might just as well be shifted with 2π in Φ_{22} since $\Phi_{22} = 0 = 2\pi$. Thus one should be careful to remember the periodicity of the signal when dealing with values of Φ_{22} very close to $0 = 2\pi$.

[19] $\Psi_n \to -\Psi_n + 2\pi$

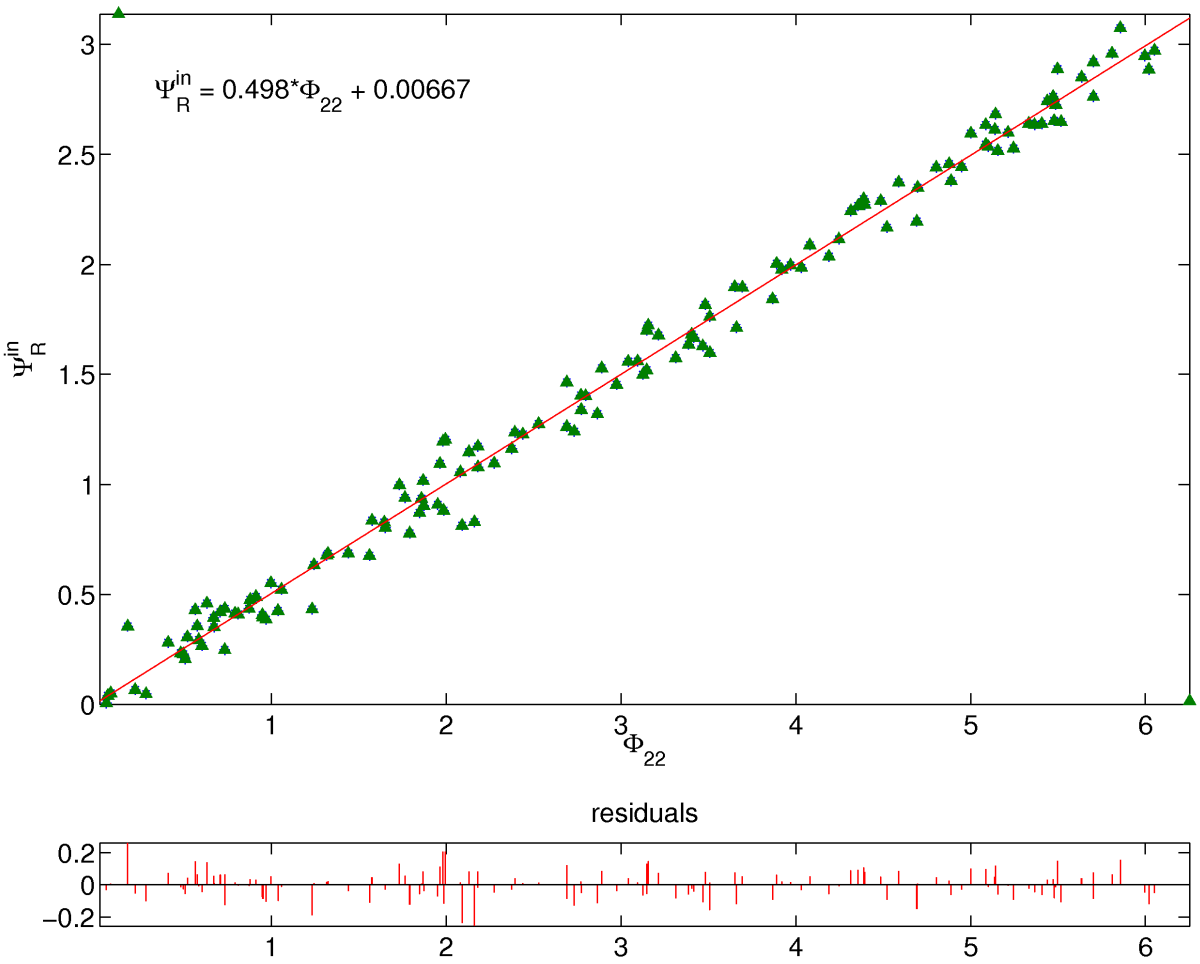

Figure 8.7: The (corrected) input Ψ_R versus Φ_{22} in radians. The equation shows the linear fit to the corrected data. A linear fit to the total dataset gives $\Psi_R^{in} = 0.456 * \Phi_{22} + 0.128$ instead.

Another thing to note is the relationship between Ψ_n and Φ_{22}

$$2\Psi_n = \Phi_{22} + 2\pi k, \qquad k = 0, 1, 2, 3, ... \tag{8.2}$$

One specifies v_2 for each simulation (ensemble of events), and the generator generates events with Ψ_R randomly chosen between 0 and 2π. In practice it is not possible to distinguish a reaction plane angle of e.g. $\frac{1}{2}\pi$ and $\frac{3}{2}\pi$ because of the symmetry[20]. Thus the event plane angle is only defined for $[0 : \pi]$ (and this is the only one observable in practice).

Because the data plotted in figure 8.7 is Φ_{22} vs. Ψ_R^{in}, a shift has been made to show the linear relationship from $[0 : \pi]$. The input Ψ_R range from $[0 : 2\pi]$ from the simulation. To correct for angles that are in praxis the same because of the symmetry explained before, the following shift was done on the data: for $\Psi_R^{in} > \pi, \rightarrow \Psi_R = \Psi_R^{in} - \pi$.

[20]see figure 4.1. The reaction plane angle is defined by the vector from nuclei "A" to nuclei "B" no matter the orientation, and it therefore spans the whole 2π interval. If the two nuclei were interchanged the event plane angle would be the same, but the reaction plane angle would be $\pm\pi$

Chapter 9

Conclusions

In this thesis a novel approach to the analysis of high-multiplicity heavy ion collisions has been presented. The approach is the use of methods and tools developed for the analysis of the Cosmic Microwave Background (CMB) in the field of cosmology, applied to the analysis of the morphology of heavy ion collisions in the field of heavy ion physics. The specific topic of investigation was elliptic flow, v_2, on an *event-by-event* basis.

The CMB analysis approach is based on the decomposition of a signal into spherical harmonics, a three dimensional fourier transformation. The coefficients of the decomposition, a_{lm}'s, encode all information of the decomposed signal, and it is thus possible to do analytical calculations on the signal using these coefficients.

Using the power spectrum obtained through the spherical harmonics coefficients, the background of a heavy ion collision signal - an event - was identified as being strongly represented by the $m = 0$ modes of the coefficients (because $m = 0$ modes are ϕ independent). Removing the $m = 0$ mode clearly removed the dominance of the background without influencing modulations in the ϕ-direction such as flow. The spherical harmonics coefficients were also used to derive equations for separation of both even and odd flow moments from the total signal, and a direct analytical expression was obtained for the isolation of flow in an event. The results show that elliptic flow is best determined from the a_{22} coefficient from the spherical harmonics decomposition.

In order to do the analysis of the heavy ion data, it was first converted to a format suitable for the CMB program package, GLESP. GLESP was used for the decomposition into spherical harmonics and the calculation of the power spectra.

The data analysis was split into two parts. The first implemented the mathematical methods on a toy model, which is based on a simple random generator. The second part extended the analysis to the more sophisticated HIJING generator, which uses physics for the generation of simulations. The analysis of the toy model data showed a very strong linear relationship between the input v_2 and the calculated v_2, as was predicted by the equations from the methods chapters (figure 7.9). A small deviation from the predicted behaviour was seen, which was ascribed to a calibration factor due to limited resolution.

The HIJING simulations were analysed in a similar way and also showed a strong linear correlation, albeit with a slope that differed with regards to the predictions (figure 8.5). The

method for analysis was the same for both toy model and HIJING, which suggests that it is improbable that the derived equations for the calculation of flow are erroneous per se. However, high fluctuations in the signal in the ϕ direction were seen for the density of particles. These prompted the investigation of the assumptions for the formula, which showed that noise is prominent in the data, and that the fraction $\frac{|a_{21}|}{|a_{22}|}$ is unexpectedly large which indicates a tilt with respect to θ of the symmetry plane in the data. Such a tilt would mimic a θ dependence of v_2, and would induce couplings of l-modes. The original equation does not take θ dependence into account, and thus cannot predict the observed behaviour perfectly. This is a possible explanation for the discrepancy. Also, the limited resolution contributes to the calibration factor. In conclusion, the linear relationship is sound, but further investigation into the origin of the tilt is needed as well as either discriminating the noise or enhancing the flow signal in the data (e.g. filters, masks, window functions).

The analysis of HIJING simulations also investigated how well the event plane angle, Ψ_n, could be reconstructed for each event. A sample of 164 events with $v_2 = 0.07$ and multiplicities $10000 \leq N_{part} < 30000$ was analysed. A plot comparing the input reaction plane angle ($\Psi_R = \Psi_2$) and the calculated event plane angle from the phase of the a_{22} coefficient, $\Psi_n = 0.5\Phi_{22}$, showed a very tight relationship completely in agreement with the analytical formula (figure 8.7). The event plane angle is not expected to be affected by effects that influence the amplitude of the flow, as it is only a shift of the distribution in ϕ.

The method presented in this thesis has proven promising for the determination of elliptic flow in heavy ion collisions on event-by-event basis. The main result is that the relationship $\frac{|a_{22}|}{|a_{20}|} = v_2$ was supported by the data for a toy model. For HIJING with afterburner the linear relationship is also confirmed albeit with a discrepancy. It has been shown that one can qualitatively characterise properties of collisions on event-by-event basis by using methods normally used in CMB science, even if a completely successful application to more advanced simulations requires either more sophisticated estimators or better reduction of the noise.

The outlook for the data analysis of this thesis has many sides to it. Firstly, the discrepancy of the HIJING simulations requires further investigation. Then one should check the method for higher order flow, for limited detector acceptance and simulations with more effects. The next step would be analysis of real data from the ALICE detector. Since the 'true' v_2 (or higher orders) and Ψ_R (Ψ_n) are not known in real data, one could compare the results to other observables known to be correlated with collective flow, e.g. the centrality. Another way could be to determine the calibration factor using a large ensemble of events with v_2 determined through usual heavy ion methods, and then using it on an event-by-event basis.

An outlook into the field of cosmology also presents possibilities. For cosmology, the study of modulations in the morphology of a signal is highly relevant for CMB investigations. Foregrounds and cosmological signatures both present themselves through a modulation of the morphology, and thus the approach presented here can - although not directly - also be applied to studies of the CMB.

List of Figures

List of Tables

Bibliography

[1] P. Naselsky, C. H. Christensen, P. R. Christensen, P. H. Damgaard, A. Frejsel, J. J. Gaardhje, A. Hansen, M. Hansen, J. Kim, O. Verkhodanov, U. A. Wiedemann, *Morphology of High-Multiplicity Events in Heavy Ion Collisions*, submitted for Phys.Rev.C., arXiv:1204.0387v1

[2] A. R. Liddle & D. H. Lyth, *Cosmological Inflation and Large Scale Structure*, Cambridge University Press, New York, 2000.

[3] D. Larson et al., *Seven-Year Wilkinson Microwave Anisotropy Probe (WMAP) Observations: Power Spectra and WMAP-Derived Parameters*, Astrophys.J.Suppl.192:16, 2011, arXiv:1001.4635v2.

[4] D. Teaney, *The Effect of Shear Viscosity on Spectra, Elliptic Flow, and HBT Radii*, Phys.Rev. C68 034913, 2003, arXiv:nucl-th/0301099v4.

[5] P. Romatschke & U. Romatschke, *Viscosity Information from Relativistic Nuclear Collisions: How Perfect is the Fluid Observed at RHIC?*, Phys. Rev. Lett. 99, 172301, 2007, arXiv:0706.1522v2.

[6] G. Hinshaw et al., *Three-Year Wilkinson Microwave Anisotropy Probe (WMAP) Observations: Temperature Analysis*, Astrophys.J.Suppl.170:288, 2007, arXiv:astro-ph/0603451v2

[7] LAMBDA website - NASA's data center for Cosmic Microwave Background (CMB) research: *http://lambda.gsfc.nasa.gov/*

[8] C. L. Bennett et al., *4-Year COBE DMR Cosmic Microwave Background Observations: Maps and Basic Results*, Astrophys.J.464:L1-L4, 1996, arXiv:astro-ph/9601067

[9] C. L. Bennett et al., *The Microwave Anisotropy Probe (MAP) Mission*, Astrophys.J.583:1-23, 2003, arXiv:astro-ph/0301158v1

[10] Planck Collaboration, *Planck: The Scientific Programme (bluebook)*, ESA-SCI(2005)1, 2005

[11] K. Land & J. Magueijo, *Is the Universe odd?*, Phys.Rev.D72:101302, 2005, arXiv:astro-ph/0507289v1.

[12] J. Kim & P. Naselsky, *Anomalous parity asymmetry of WMAP 7 year power spectrum data at low multipoles: is it cosmological or systematics?*, PhysRevD.82.063002, 2010, arXiv:1002.0148.

[13] C. L. Bennett et al., *Seven-Year Wilkinson Microwave Anisotropy Probe (WMAP) Observations: Are There Cosmic Microwave Background Anomalies?*, Astrophys.J.Suppl.192:17, 2011, arXiv:1001.4758v2.

[14] B. Ryden, *Introduction to cosmology*, Addison Wesley, San Francisco, 2003.

[15] A. Linde, *Inflationary Cosmology*, Lect. Notes Phys. 738, 1-54, 2008, Springer-Verlag, Berlin Heidelberg, 2008.

[16] Website for the Planck Mission: *http://sci.esa.int/science-e/www/area/index.cfm?fareaid=17*

[17] J. A. Tauber et al. (Planck Collaboration), *Planck pre-launch status: The Planck mission*, A&A 520 A1, 2010.

[18] A. Lewis & A. Challinor, *Code for Anisotropies in the Microwave Background (CAMB)*, http://camb.info/

[19] A. Lewis & S. Bridle, *Cosmological parameters from CMB and other data: a Monte-Carlo approach*, Phys.Rev.D66:103511, 2002, arXiv:astro-ph/0205436v3.

[20] E. Komatsu et al., *Seven-year Wilkinson Microwave Anisotropy Probe (WMAP) Observations: Cosmological Interpretation*, Astrophys.J.Suppl.192:18, 2011, arXiv:1001.4538v3.

[21] S. L. Bridle, A. M. Lewis, J. Weller & G. Efstathiou, *Reconstructing the primordial power spectrum*, Mon.Not.Roy.Astron.Soc. 342 L72, 2003, arXiv:0302306.

[22] D. Scott & G. Smoot, *Cosmic Microwave Background Mini-Review*, Phys.Lett.B 592, 2004, arXiv:astro-ph/0406567.

[23] D. Larson et al., *Seven-year Wilkinson Microwave Anisotropy Probe (WMAP) Observations: Power*
Spectra and WMAP Derived Parameters, Astrophys.J.Suppl.192:16,2011,
arXiv:1001.4635v2.

[24] S. Dodelson *Modern Cosmology*, Academic Press, US, 2003

[25] K. Land & J. Magueijo, *The Axis of Evil*, Phys.Rev.Lett.95:071301, 2005, arXiv:astro-ph/0502237v2.

[26] M. Gyulassy & L. McLerran, *New Forms of QCD Matter Discovered at RHIC*,
Nucl.Phys.A750:30-63, 2005, arXiv:nucl-th/0405013v2.

[27] J. Letessier & J. rafelski, *Hadrons and quark-gluon plasma*, Cambridge Monographs on Particle Physics, Nuclear Physics and Cosmology no. 18, Cambridge University Press, UK, 2004

[28] A. M. Poskanzer & S. A. Voloshin, *Methods for analyzing anisotropic flow in relativistic nuclear collisions*, Phys.Rev.C58:1671-1678, 1998, arXiv:nucl-ex/9805001v2

[29] S. Voloshin and Y. Zhang, *Flow Study in Relativistic Nuclear Collisions by Fourier Expansion of Azimuthal Particle Distributions*, Z.Phys.C70:665-672, 1996, arXiv:hep-ph/9407282v1.

[30] M. L. Miller et al., *Glauber modeling in high energy nuclear collisions*, Ann.Rev.Nucl.Part.Sci. 57:205-243, 2007, arXiv:nucl-ex/0701025

[31] B.R. Martin & G. Shaw, *Particle Physics*, third edition, Wiley, UK, 2008.

[32] The ATLAS Collaboration, *Title: Observation of a Centrality-Dependent Dijet Asymmetry in Lead-Lead Collisions at sqrt(S(NN))= 2.76 TeV with the ATLAS Detector at the LHC*, Phys.Rev.Lett.105:252303, 2010, arXiv:1011.6182v2.

[33] J.-Y. Ollitrault, *Anisotropy as a signature of transverse collective flow*, Phys. Rev. D 46, 229245, 1992.

[34] S.A. Voloshin, A. M. Postkanzer & R. Snellings, *Collective phenomena in non-central nuclear collisions* from the book Landolt-Boernstein *Relativistic Heavy Ion Physics, Vol. 1/23, p 5-54.*, Springer-Verlag, 2010, arXiv:0809.2949.

[35] K. Aamodt et al. (ALICE Collaboration), *Elliptic Flow of Charged Particles in Pb-Pb Collisions at* $\sqrt{s_{NN}}$*=2.76TeV*, Phys.Rev.Lett.105.252302, 2010, arXiv:1011.3914v2

[36] ATLAS Collaboration, *Measurement of the azimuthal anisotropy for charged particle production in* $\sqrt{s_{NN}}$ *= 2.76 TeV lead-lead collisions with the ATLAS detector*, Submitted to Phys.Rev.C., 2012, arXiv:1203.3087v2

[37] D. Teaney, *Viscous Hydrodynamics and the Quark Gluon Plasma*, 2009, arXiv:0905.2433v1.

[38] P. Romatschke, *New Developments in Relativistic Viscous Hydrodynamics*, Int.J.Mod.Phys.E 19 1-53, 2010, arXiv:0902.3663v3.

[39] B. Alver & G. Roland, *Collision-geometry fluctuations and triangular flow in heavy-ion collisions*, Phys.Rev.C81:054905, 2010, arXiv:1003.0194v3.

[40] P. Sorensen, *Implications of spacemomentum correlations and geometric fluctuations in heavy-ion collisions*, J.Phys.G: Nucl.Part.Phys.37:094011, 2010.

[41] A. Adare et al. (PHENIX Collaboration), *Measurements of Higher Order Flow Harmonics in Au+Au Collisions at* $\sqrt{s_{NN}} = 200GeV$, Phys.Rev.Lett.107:252301, 2011.

[42] K. Aamodt et al. (ALICE Collaboration), *Higher harmonic anisotropic flow measurements of charged particles in Pb-Pb collisions at 2.76 TeV*, Phys.Rev.Lett.107:032301, 2011, arXiv:1105.3865v2.

[43] B. Alver, C. Gombeaud, M. Luzum & J.-Y. Ollitrault, *Triangular flow in hydrodynamics and transport theory*, Phys.Rev.C82:034913, 2010, arXiv:1007.5469v2.

[44] R. S. Bhalerao, M. Luzum & J.-Y. Ollitrault, *Determining initial-state fluctuations from flow measurements in heavy-ion collisions*, Phys.Rev.C84:034910, 2011, arXiv:1104.4740v2.

[45] Edited by A. Breskin & R. Voss, *The CERN Large Hadron Collider: Accelerator and Experiments*, Volume 1 and 2, CERN, 2009

[46] P. Naselsky, M. Hansen & J. Kim, *Symmetry of the CMB sky as a new test of its statistical isotropy. Non Cosmological Octupole?*, 2011, arXiv:1105.4426v4

[47] K. F. Riley, M. P. Hobson & S. J. Bence, *Mathematical Methods for Physics and Engineering*, second edition, Cambridge University Press, UK, 2002.

[48] J. R. Taylor, *An Introduction to Error Analysis*, 2nd edition, University Science Books, US, 1997

[49] A. G. Doroshkevich et al., *Gauss-Legendre Sky Pixelization (GLESP) scheme for CMB maps*, International Journal of Modern Physics D, Vol.14 No.2 pp. 275-290, 2005, arXiv:0305537.

[50] A. G. Doroshkevich et al., *The Gauss-Legendre Sky Pixelization for the CMB polarization (GLESP-pol). Errors due to pixelization of the CMB sky*, Int.J.Mod.Phys.D20:1053-1078, 2011, arXiv:0904.2517v1

[51] Rene Brun & Fons Rademakers, *ROOT - An Object Oriented Data Analysis Framework.*, Nucl. Inst. & Meth. in Phys. Res. A, 389, 81, 1997.

[52] X.-N. Wang & M. Gyulassy, *HIJING: A Monte Carlo model for multiple jet production in p p, p A and A A collisions*, Phys.Rev.D44 3501-3516, 1991

Appendices

Appendix A

Fourier decomposition

A.1 Cylindrical fourier decomposition

In cylindrical coordinates the signal from a collision is represented by:

$$S(z,\phi) = R(z,\phi)\left(1 + 2\sum_{n\geq 1} v_n \cos(n[\phi - \Psi_n])\right), \tag{A.1}$$

as defined in Eq.(4.3). The fourier decomposition in ϕ is done by

$$R_m(z) = \int_{-\pi}^{\pi} R(z,\phi)e^{-im\phi}d\phi, \tag{A.2}$$

and by using that

$$\cos(nx) = \frac{e^{inx} + e^{-inx}}{2}. \tag{A.3}$$

The decomposed signal is then given by

$$\begin{aligned}
S_m(z) &= R_m(z) + 2\int_{-\pi}^{\pi} R(z,\phi)\sum_n v_n \cos(n[\phi - \Psi_n])e^{-im\phi}d\phi \\
&= R_m(z) + \sum_n v_n\left(\int_{-\pi}^{\pi} R(z,\phi)e^{in(\phi-\Psi_n)}e^{-im\phi}d\phi + \int_{-\pi}^{\pi} R(z,\phi)e^{-in(\phi-\Psi_n)}e^{-im\phi}d\phi\right) \\
&= R_m(z) + \sum_n v_n\left(e^{-in\Psi_n}\int_{-\pi}^{\pi} R(z,\phi)e^{-i\phi(m-n)}d\phi + e^{in\Psi_n}\int_{-\pi}^{\pi} R(z,\phi)e^{-i\phi(m+n)}d\phi\right) \\
&= R_m(z) + \sum_n v_n\left(e^{-in\Psi_n}R_{m-n}(z) + e^{in\Psi_n}R_{m+n}(z)\right).
\end{aligned} \tag{A.4}$$

A.2 Decomposition in spherical coordinates

$$\begin{aligned}
\int_\Omega S(\theta,\phi)Y^*_{l'm'}d\Omega &= \int_\Omega R(\theta,\phi)Y^*_{l'm'}d\Omega + \sum_n v_n\int_\Omega R(\theta,\phi)e^{in(\phi-\Psi_n)}Y^*_{l'm'}(\theta,\phi)d\Omega \\
&\quad + \sum_n v_n\int_\Omega R(\theta,\phi)e^{-in(\phi-\Psi_n)}Y^*_{l'm'}(\theta,\phi)d\Omega \Leftrightarrow
\end{aligned} \tag{A.5}$$

$$
\begin{aligned}
a_{lm} &= c_{lm} + \sum_n v_n e^{-in\Psi_n} \int_\Omega \sum_{l,m} c_{lm} Y_{lm}(\theta,\phi) Y^*_{l'm'}(\theta,\phi) e^{in\phi} d\Omega \\
&\quad + \sum_n v_n e^{in\Psi_n} \int_\Omega \sum_{l,m} c_{lm} Y_{lm}(\theta,\phi) Y^*_{l'm'}(\theta,\phi) e^{-in\phi} d\Omega \\
&= c_{lm} + \sum_n v_n e^{-in\Psi_n} \int_0^\pi \sum_{l,m} c_{lm} K P_{lm}(\cos\theta) K' P_{l'm'}(\cos\theta) \sin\theta d\theta \int_{-\pi}^{\pi} e^{i\phi(m+n-m')} d\phi \\
&\quad + \sum_n v_n e^{in\Psi_n} \int_0^\pi \sum_{l,m} c_{lm} K P_{lm}(\cos\theta) K' P_{l'm'}(\cos\theta) \sin\theta d\theta \int_{-\pi}^{\pi} e^{i\phi(m-n-m')} d\phi \\
&= c_{lm} + \sum_n v_n c_{lm} \left(e^{-in\Psi_n} \frac{1}{2\pi} \delta_{l,l'} \delta_{m,m'} 2\pi \delta_{m',m+n} + e^{in\Psi_n} \frac{1}{2\pi} \delta_{l,l'} \delta_{m,m'} 2\pi \delta_{m',m-n} \right) \\
&= c_{lm} + \sum_n v_n \left(c_{l,m+n} e^{-in\Psi_n} + c_{l,m-n} e^{in\Psi_n} \right), \qquad \text{(A.6)}
\end{aligned}
$$

where

$$
\begin{aligned}
K &= \sqrt{\frac{(l-m)!}{(l+m)!} \frac{2l+1}{4\pi}}, \\
K' &= \sqrt{\frac{(l'-m')!}{(l'+m')!} \frac{2l'+1}{4\pi}}, \qquad \text{(A.7)}
\end{aligned}
$$

and

$$
\int_0^\pi K P_{lm}(\cos\theta) K' P_{l'm'}(\cos\theta) \sin\theta d\theta = \frac{1}{2\pi} \delta_{l,l'} \delta_{m,m'}. \qquad \text{(A.8)}
$$

Appendix B

GLESP commands

The command used for making a map is

mappat -A ALICE_input.txt -o ALICE_map.fits -nx 201 -np 402

The flags $-nx$ and $-np$ define the resolution of the map. $-nx$ is the resolution in θ and $-np$ is the resolution in ϕ. The relationships $nx \geq 2 * l_{max} + 1$ and $np = 2 * nx$ must be fulfilled; In this analysis $l_{max} = 100$.

After making a map, the decomposition into spherical harmonics (and coefficients) is done by the command $cl2map$. $cl2map$ can make maps from a power spectrum or a list of a_{lm}s, or compute the power spectrum or a_{lm}s from a map. $alm2dl$ does calculations on a_{lm}s. It can also convert a alm.fits file to ASCII format. Here $cl2map$ is used to find the spherical harmonics coefficients from the ALICE map, and $alm2dl$ is used to produce the corresponding power spectrum and a ASCII file of the a_{lm}s.

cl2map -map ALICE_map.fits -lmax 100 -ao alm.fits

decomposes a map into a_{lm}s.

alm2dl -cl alm.fits -lmax 100 -o cl.fits

computes the power spectrum from a list of a_{lm}s.

alm2dl -g alm.fits -o alm.dat

converts a list of a_{lm}s in fits format to ASCII format.

To produce a figure from a map the command $f2fig$ is used. The flag $-Cs$ allows for manual determination of the temperature range (in this case, particle counts).

f2fig map.fits -o map.gif -Cs Low,High

where Low and High are the limits.